IN-24
185369
50P

NASA Contractor Report 189136

Thermal Shock Resistance of Ceramic Matrix Composites

D.M. Carper
GE Aircraft Engines
Cincinnati, Ohio

and

H.F. Nied
GE Corporate Research and Development
Schenectady, New York

August 1993

Prepared for
Lewis Research Center
Under Contract NAS3–25640

National Aeronautics and
Space Administration

(NASA-CR-189136) THERMAL SHOCK RESISTANCE OF CERAMIC MATRIX COMPOSITES Final Report (GE) 50 p

N94-13920

Unclas

G3/24 0185369

ABSTRACT

This report details the experimental and analytical investigation of the thermal shock phenomena in ceramic matrix composites. The composite systems examined were oxide-based, consisting of an aluminosilicate matrix with either polycrystalline aluminosilicate or single crystal alumina fiber reinforcement. The program was divided into three technical tasks; baseline mechanical properties, thermal shock modeling, and thermal shock testing.

The analytical investigation focused on the development of simple expressions for transient thermal stresses induced during thermal shock. The effect of various material parameters, including thermal conductivity, elastic modulus, and thermal expansion, were examined analytically for their effect on thermal shock performance. Using a simple maximum stress criteria for each constituent, it was observed that fiber fracture would occur only at the most extreme thermal shock conditions and that matrix fracture, splitting parallel to the reinforcing fiber, was to be expected for most practical cases.

Thermal shock resistance for the two material systems was determined experimentally by subjecting plates to sudden changes in temperature on one surface while maintaining the opposite surface at a constant temperature. This temperature change was varied in severity (magnitude) and in number of shocks applied to a given sample. The results showed that for the most severe conditions examined that only surface matrix fracture was present with no observable fiber fracture. The impact of this damage on material performance was limited to the matrix dominated properties only. Specifically, compression strength was observed to decrease by as much as 50% from the measured baseline.

FOREWORD

This is the Final Report covering the activities performed under NASA Contract NAS3-25640, "Thermal Shock Resistance of Ceramic Matrix Composites". It was prepared by the Engineering Materials Technology Laboratories (EMTL) of GE Aircraft Engines, Cincinnati, Ohio. Mr. D.M. Carper was the GE Program Manager and Dr. H.F. Nied, GE Corporate Research and Development, conducted the analytical treatment of the thermal shock phenomenon. Dr. M.J. Hyatt was the Project Manager for NASA Lewis Research Center.

Table of Contents

List of Tables

List of Figures

List of Figures
(Continued)

1.0 INTRODUCTION

The use of high temperature, lightweight materials is essential in order to meet the performance objectives of the 21st Century gas turbine engine. This has provided the impetus to the development of advanced high temperature composites and, as a result, considerable progress has been made in the last decade. Of the candidate materials, only carbon-carbon and ceramic matrix composites are considered to have potential for operation at temperatures in excess of 1350 C.

A potentially life-limiting factor for high temperature components is the thermal shock commonly experienced during engine cycling. While the thermal shock resistance of carbon-carbon is quite good, the lack of environmental stability precludes its evaluation in this program. Ceramic matrix composites (CMC's), on the other hand, have a wide range of thermal properties which can influence thermal shock behavior. Unlike monolithic ceramics, which perform poorly when subjected to thermal shock, CMC's exhibit higher inelastic strains and more graceful failure morphology due to deflection of cracks by the reinforcing fibers. While families of CMC's with lower thermal conductivity are typically considered to have lower thermal shock resistance, the improved toughness may provide enhanced thermal shock resistance.

This program was funded by NASA-LeRC under the HITEMP initiative and was aimed at determining the applicability of oxide-based ceramic composites in long-life, high temperature components of advanced civil aircraft engines. GEAE focused on determining thermal shock damage mechanisms, determining the material properties which influence thermal shock resistance, and assessing various thermomechanical relationships that describe the thermal shock behavior of two oxide/oxide CMC's, developed by GE for 1000 C and 1300 C applications. This was accomplished in three tasks in which the initial properties of the materials were determined (Task I), the thermal shock resistance of the two systems evaluated experimentally (Task II), and an analytic description of the thermal shock process developed (Task III).

2.0 Experimental Procedure

2.1 Material Systems Description

The two material systems examined in this program were a Sumitomo (polycrystaline aluminosilicate) reinforced aluminosilicate and a sapphire (single crystal alumina) reinforced aluminosilicate. These systems have been selected by GEAE because of their exceptional high temperature environmental stability and their good elevated temperature properties. While the mechanical performance of these systems are quite good (strengths of 70 - 140 MPa at their respective use temperatures), the thermal conductivity of the systems are low (less than 2 W/m•K) ; thus, both systems may be susceptible to thermal shock damage.

The two oxide-based material systems were fabricated via a GEAE developed technique in which fiberous preforms are infiltrated with a ceramic containing slurry (Figure 1). The slurry, containing ceramic powders and polymeric binders, is infiltrated into the preform to yield a pre-preg. This ceramic pre-preg has many of the same attributes found in polymeric pre-pregs where sufficient drape and tack are present to allow for fabrication of complex shapes. As with polymeric composites, laminates are formed by stacking plies of pre-preg and curing under modest heat (~150 C) and pressure (~1.5 MPa). After lamination, organics are removed during an intermediate temperature firing and the laminate is pressureless sintered in air to yield the final ceramic composite. During this sintering operation, the polymeric binders decompose and react with the ceramic powders to form an alumina-rich mullite. Mineral additions are included in the slurry pre-preg to control shrinkage during sintering.

2.2 Mechanical Test Procedures

In order to assess the effect of thermal shock on the CMC's studied in this program, mechanical and thermal testing was conducted on unshocked material to establish baseline performance. This testing included determination of tensile, compressive, and shear properties, as well as thermal conductivity and thermal expansion. Testing on the Sumitomo reinforced aluminosilicate was conducted at temperatures up to 1100 C while the sapphire system was evaluated at temperatures up to 1300 C.

Tensile tests were performed using a technique similar to ASTM D3039. The test set-up consisted of a servo-hydraulic load frame configured with hydraulically actuated grips, which have been shown to provide greater load train alignment than is possible with more conventional gripping methods (Figure 2). Specimen heating was accomplished with a SiC susceptor which provided for a 25 to 38 mm uniform hot zone. A modified high temperature extensometer with a 12 mm gage length acquired strain measurements within this uniformly heated gage section. The specimen geometry was straight-sided and untabbed.

Compression testing was performed with a modified ASTM D695 technique, which constrains the specimen from buckling during testing. To allow for testing at temperature up to 1300 C, modifications were made to the test fixturing, including the substitution of SiC for the fixture material. The conventional D695 fixturing consists of a double cruciform in which the specimen is constrained (Figure 3a). This approach was believed to be inadequate at elevated temperature as the mismatch in thermal growth between specimen and fixturing may be significant. GEAE developed a "V"-block fixture (Figure 3b) which allows for the same side constraint as the conventional D695 fixture with the ability to engage the side constraints at elevated temperature.

In-plane and interlaminar shear properties were also determined. The in-plane shear properties were determined through a combination of ±45 tensile tests, at room and elevated temperature, and Iosipescu shear tests at room temperature. The ± 45 tensile tests were performed using the procedure described in ASTM D3518. The interlaminar shear strength of the composites were determined from compressive double-notch shear tests at both room and elevated temperature. The test procedure was identical to that used for the compression testing and specimen configuration is shown in Figure 4. Also, interlaminar tensile strength at room temperature was measured utilizing a technique similar to ASTM C297. Fixturing consisted of titanium tabs bonded to the ceramic composite using a low temperature cure epoxy adhesive (Figure 5).

2.3 Thermal Shock Testing

Three thermal shock conditions were evaluated for this study. The conditions examined were; shock-down, where an initially hot body is subjected to sudden cooling, shock-up, where a cool body is subjected to rapid heating, and planar shock, where a cool body is subjected to a high in-plane thermal transient. All of the conditions examined are of great interest in gas turbine design as start-up and shut-down, in addition to several other conditions, may give rise to the shock-up and shock-down conditions, and non-symmetrical heating ("hot streaks") is commonplace. Typically, thermal shock testing is accomplished through burner rig testing of small buttons of material. This technique does not allow for post-shock mechanical characterization to determine the extent of property degradation, nor does it allow for accurate determinations of shock conditions, such as severity of the applied shock. The approach taken in this study was to utilize a technique which would supply a controlled, uniform thermal shock to a sample which could then be subjected mechanical tests to determine performance characteristics.

To evaluate the shock-down condition, a two-zone furnace (Figure 6) was modified to provide a blast of chilled air to the surface of a heated specimen. This was accomplished through modification of the furnace elevator design to provide rapid descent into the "cooling" zone of the furnace. An air delivery system, consisting of an actuating nozzle to provide for directed flow and a liquid nitrogen injector to chill the air and provide for a two-phase media, was added to the furnace to improve the capability of the system. Constant backside temperature was maintained through the use of a large, insulated SiC holding fixture which, due to its large thermal mass, maintained nearly constant backside temperature on the sample through the shock application. A schematic of the test apparatus is also shown in Figure 6. Preliminary testing was conducted on instrumented CMC samples to determine heat transfer conditions and to determine the uniformity of the resulting temperature distribution. The results of this testing show the most severe shock attainable, with a fully extended nozzle and liquid nitrogen injection, provided a through thickness thermal gradient of approximately 150 F after 5 seconds of exposure. Compared to a typical burner rig, which may yield thermal gradients of 260 - 520 C in 5 seconds, the thermal shock was not severe; however, the uniformity of the thermal gradient allowed for determination of post-shock performance.

The shock-up condition was evaluated through the application of rapid heating, accomplished by bringing an initially cool body into contact with a hot body (Figure 7). Near constant backside temperature was accomplished by attaching the test sample to a water cooled copper heat sink. The severity of thermal shock attained in this configuration was greatly improved over the shock-down configuration. Thermal gradients of in excess of 520 C were obtained after 5 seconds, thus comparing favorably with burner rig tests.

Planar shock was evaluated by using a test set-up which provided line heating of both top and bottom surfaces of the test sample (Figure 8). Accurate measurement of the thermal gradient was not possible due to limitations in instrumentation, namely resolution of the pyrometer used to determine surface temperature; however, gradients appeared to have been at least 100 - 150 C over a 6 mm span. This magnitude of planar thermal gradient closely approximates typical "hot streak" conditions observed in engine testing.

Upon establishing the heat transfer conditions in each of the test configurations, test samples were exposed to cyclic shock applications under either "severe" conditions or "moderate" conditions. Severe conditions maximized the heat transfer coefficient for the various systems while the moderate conditions were performed at ~2/3 the heat transfer coefficient of the severe case. The samples, 32 mm x 127 mm, were examined optically both prior and subsequent to testing to document any obvious damage due to thermal shock. Mechanical test specimens were then extracted for post-shock testing. Finally, representative samples were evaluated for any changes in microstructure.

2.4 Analytical Treatment

To gain further insight into the thermal shock phenomena in CMC's, analytic solutions were derived for the transient thermal stress problem in an orthotropic media. The configuration studied was a thin CMC plate with undirectional fiber reinforcement. For the purposes of this analysis, it was assumed that the CMC could be modelled as a homogeneous plate. To compare with experimental results, the applied temperature was assumed to be uniform across the upper surface of the plate and that heat flux was lost from the surface by convection to the environment.

The steady-state thermoelastic analysis of a finite orthotropic slab has been studied by Akoz and Tauchert (1978), and Wang and Chou (1984, 1985) have dealt with the transient problem. All these papers considered the 2-D case, where the temperaturte does not vary in the transverse direction, and either plane-stress or plane-strain condition can be used for the stress analysis.

The uni-directional sample is modelled as a homogeneous plate, as depicted in Figure 9. The plate can be considered to be both thermally and elastically orthotropic. As will be shown, since the actual sample has a large length:thickness ratio, and due to symmetry of the applied temperature, the temperature distribution may be considered to be 1-dimensional sufficiently away from the ends of the sample. Results from a simple finite element analysis confirm this, and these results are presented graphically in Section 4.3. The solutions of Akoz and Tauchert (1978), and Wang and Chou (1984, 1985) do not give the complete thermal solutions for the situation when the applied thermal shock is uniform, since integral terms in their temperature solutions become zero in certain cases under this condition.

The thermal stress components in the central region of the sample may be reduced to two plane strain problems for the orthotropic strip, and are derived in Section 4.2. However, these two problems are not totally independent since there is an inherent coupling between material properties for an orthotropic material. For a general orthotropic material there exist nine independent elastic constants, three independent coefficients of thermal conductivity, and three independent coefficients of thermal expansion. The material properties used for the calculations discussed in this report are given in Table 1.

2.4.1 Thermal Analysis

Initially, the temperature of the slab is T_0 and at time t, the temperature of the slab at point (x,y) is given by $\Theta(x,y;t)$. The relative temperature distribution at time t is given by

$$T(x,y;t) = \Theta(x,y;t) - T_0. \tag{1.1}$$

The two-dimensional temperature distribution is assumed to be governed by the transient heat conduction equation

$$\frac{\partial^2 T}{\partial x^2} + K^2 \frac{\partial^2 T}{\partial y^2} = \frac{1}{D_x} \frac{\partial T}{\partial t} \tag{1.2}$$

where $K^2=K_y/K_x$, the ratio of the thermal conductivity in the y direction to the thermal conductivity in the x direction. D_x is the thermal diffusivity in the x direction and is given by $D_x=K_x/c\rho$ where c is the specific heat of the material and ρ is the mass density of the material. The thermal diffusivity in the y direction is denoted by D_y.

As boundary conditions on the three sides of the rectangle, the general equations governing linear heat transfer may be used:

$$-a_1 \frac{\partial T}{\partial x} + b_1 T = 0 \qquad \text{for } x = 0$$

$$a_2 \frac{\partial T}{\partial x} + b_2 T = 0 \qquad \text{for } x = L_1$$

$$-a_3 \frac{\partial T}{\partial y} + b_3 T = 0 \qquad \text{for } y = 0$$

where the a_i are conductivities and the b_i are the surface heat transfer coefficients. On the upper surface ($y=L_2$) a more general, inhomogeneous condition is allowed:

$$a_4 \frac{\partial T}{\partial y} + b_4 T = f(x) \qquad \text{for } y = L_2 \tag{1.3}$$

By appropriate selections of a_i and b_i, various general types of boundary conditions may be obtained, with the simplest forms being zero applied temperature (a=0) and zero flux change (b=0). Although the equations are set up for a non-homogeneous condition on one side only, a more complicated system of boundary conditions may be analyzed through an appropriate system of coordinate rotation, and a subsequent superposition of solutions.

As outlined by Wang and Chou (1984, 1985), since the problem has a steady-state solution as $t \to \infty$, we may separate out this solution, and express $T(x,y;t)$ in the form

$$T(x,y;t) = \phi(x,y) + \psi(x,y;t) \tag{1.4}$$

$\phi(x,y)$ then satisfies the steady state equation

$$\frac{\partial^2 \phi}{\partial x^2} + K^2 \frac{\partial^2 \phi}{\partial y^2} = 0 \tag{1.5}$$

while $\psi(x,y;t)$ satisfies the transient equation

$$\frac{\partial^2 \psi}{\partial x^2} + K^2 \frac{\partial^2 \psi}{\partial y^2} = \frac{1}{D_x}\frac{\partial T}{\partial t} \tag{1.6}$$

The general forms of the solutions of equation (1.5) may be expressed as

$$\begin{aligned}\phi(x,y) = \sum_{n=0}^{n=\infty} [&A_1(p_n)\sin(p_n x)\sinh(\frac{p_n y}{K}) + A_2(p_n)\sin(p_n x)\cosh(\frac{p_n y}{K}) \\ &+ A_3(p_n)\cos(p_n x)\sinh(\frac{p_n y}{K}) + A_4(p_n)\cos(p_n x)\cosh(\frac{p_n y}{K})]\end{aligned} \tag{1.7}$$

with boundary conditions

$$\begin{aligned}
-a_1\frac{\partial \phi}{\partial x} + b_1\phi &= 0 && \text{for } x = 0 \\
a_2\frac{\partial \phi}{\partial x} + b_2\phi &= 0 && \text{for } x = L_1 \\
-a_3\frac{\partial \phi}{\partial y} + b_3\phi &= 0 && \text{for } y = 0 \\
a_4\frac{\partial \phi}{\partial y} + b_4\phi &= f(x) && \text{for } y = L_2
\end{aligned} \tag{1.8}$$

and the corresponding transient solution of (1.6) is given by

$$\begin{aligned}\psi(x,y) = \sum_{m=0}^{m=\infty}\sum_{n=0}^{n=\infty} [&\overline{A}_1(\nu_n,\mu_m)\sin(\nu_n x)\sin(\frac{\mu_m y}{K}) + \overline{A}_2(\nu_n,\mu_m)\sin(\nu_n x)\cos(\frac{\mu_m y}{K}) \\ &+ \overline{A}_3(\nu_n,\mu_m)\cos(\nu_n x)\sin(\frac{\nu_m y}{K}) + \overline{A}_4(\nu_n,\mu_m)\cos(\nu_n x)\cos(\frac{\nu_m y}{K})] \\ &\times \exp[-D_x(\nu_n^2 + \mu_m^2)t]\end{aligned} \tag{1.9}$$

with boundary conditions

$$\begin{aligned}
-a_1\frac{\partial \psi}{\partial x} + b_1\psi &= 0 && \text{for } x = 0 \\
a_2\frac{\partial \psi}{\partial x} + b_2\psi &= 0 && \text{for } x = L_1 \\
-a_3\frac{\partial \psi}{\partial y} + b_3\psi &= 0 && \text{for } y = 0 \\
a_4\frac{\partial \psi}{\partial y} + b_4\psi &= 0 && \text{for } y = L_2
\end{aligned} \tag{1.10}$$

The initial condition is

$$\psi(x,y;0) = -\phi(x,y) \tag{1.11}$$

The coefficients $A_i(p_n)$ and $A_i(\nu_n,\mu_m)$ $(i=1,2,3,4)$ are determined from the thermal boundary conditions on the slab.

Substituting (1.7) into (1.8a-b) leads to

$$a_1 p_n A_1(p_n) + b_1 A_3(p_n) = 0$$

$$-a_1 p_n A_2(p_n) + b_1 A_4(p_n) = 0$$

$$A_1(p_n)[a_2 p_n \cos(p_n L_1) + b_2 \sin(p_n L_1)] - A_3(p_n)[a_2 p_n \sin(p_n L_1) - b_2 \cos(p_n L_1)] = 0$$

$$A_2(p_n)[a_2 p_n \cos(p_n L_1) + b_2 \sin(p_n L_1)] - A_4(p_n)[a_2 p_n \sin(p_n L_1) - b_2 \cos(p_n L_1)] = 0$$

while (1.8c) gives

$$-\frac{p_n}{K} a_3 A_1(p_n) + b_3 A_2(p_n) = 0$$

$$-\frac{p_n}{K} a_3 A_3(p_n) + b_3 A_4(p_n) = 0 \tag{1.12}$$

with similar conditions for the $A_i(\nu_n,\mu_m)$

On the upper surface $y=L_2$, it is assumed that the heat flux is removed by convectionto the environment. If the ambient temperature is constant (T_a for example) this condition may be expressed in the form

$$K_y \frac{\partial \Theta}{\partial y}(x, L_2; t) = h[T_a - \Theta(x, L_2; t)] \tag{1.13}$$

where h is the heat transfer coefficient. Equivalently the boundary condition may be expressed in terms of the relative temperature $T(x,y;t)$ as

$$\frac{\partial T}{\partial y}(x, L_2; t) + \frac{h}{K_y} T(x, L_2; t) = \frac{h}{K_y}(T_a - T_o) \tag{1.14}$$

This equation is equivalent to (1.3d), with a_4, $b_4=h/K_y$ and $f(x)$ constant and equal to $h(T_a-T_o)/K_y$.

As previously mentioned, the geometry under consideration is such that the temperature and stress fields approximate closely to a 1-dimensional state sufficiently far away from the ends of the slab. From the temperature point of view, this state is equivalent to a zero thermal flux boundary condition on the surfaces $x=0$, L_1, or alternatively, to setting $b_1=b_2=0$ in (1.8a-b) and (1.10a-b). Using (1.12a-b) it is clear that this condition leads to

$$A_1 = A_2 = 0 \tag{1.15}$$

This result implies that the temperature solution is an even function of x, which must be the case as the solution is known to be one dimensional.

When the temperature is unchanged on the lower surface ($a_3=0$), equation (1.12f) leads to

$$A_4 = 0 \tag{1.16}$$

while (1.12c) gives

$$A_3 \sin p_n L_1 = 0 \qquad \text{for } n = 0,1,2,\ldots\infty \tag{1.17}$$

Therefore, from (1.17), a non-trivial solution to (1.7) and (1.8a-c) may be obtained only if

$$p_n = \frac{n\pi}{L_1} \qquad \text{for } n = 0,1,2,\ldots\infty \tag{1.18}$$

The remaining boundary condition (1.8d) may be expressed as

$$\sum_{n=0}^{n=\infty}\left[\frac{p_n}{K}\cosh\frac{p_n L_2}{K} + \frac{h}{K_y}\sinh\frac{p_n L_2}{K}\right]A_3(p_n)\cos p_n x = \frac{h}{K_y}(T_a - T_o) \tag{1.19}$$

By multiplying both sides of (1.19) by $\cos(p_n x)$ and integrating over the range $0< x < L_1$, it is found that the only solution of (1.19) is the trivial solution $A_3(p_n)=0$ for all n. However, a temperature distribution linear in x and y is always a solution to the steady-state equation (1.5), but in many cases is invalid due to the boudary conditions. Note that the solutions given by Akoz and Tauchert (1978) and Wang and Chou (1984, 1985) do not mention the linear solution. The integral solutions they give for the coeffients A_3 are zero when the function f(x) is constant. In fact the steady-state solution of (1.5) satisfying the boundary conditions is

$$\phi(x,y) = \beta_y \frac{(T_a - T_0)}{1 + \beta_y}\left(\frac{y}{L_2}\right) \tag{1.20}$$

where β_y is taken to be the non-dimensional Biot number

$$\beta_y = \frac{hL_2}{K_v}.$$

Following a similar route, it is found that the solution to the transient part of the thermal equation reduces to

$$\psi(x,y;t) = \sum_{m=0}^{m=\infty}\sum_{n=0}^{n=\infty} \bar{A}_3(\nu_n,\mu_m)\cos(\nu_n x)\sin\left(\frac{\mu_m y}{K}\right)\exp[-D_x(\nu_n^2 + \mu_m^2)t] \tag{1.21}$$

where

$$\nu_n = \frac{n\pi}{L_1} \qquad n = 0,1,2,\ldots\ldots\infty \tag{1.22}$$

For convenience, $A_3(\nu_n,\mu_m)$ will be renamed A_{nm}. Using (1.20) and (1.21) the initial condition (1.11) can be expressed as

$$\psi(x,y;0) = \sum_{m=0}^{m=\infty}\sum_{n=0}^{n=\infty} \overline{A}_{nm}\cos(\nu_n x)\sin\left(\frac{\mu_m y}{K}\right) = -\beta_y \frac{(T_a - T_0)}{1+\beta_y}\left(\frac{y}{L_2}\right) \tag{1.23}$$

Multiplying both sides of (1.23) by $\cos(\nu_n x)$ and integratin over the range $0<x<L_1$, it is found that A_{nm} is always zero, unless ν_n is zero. Equation (1.23) then reduces to

$$\psi(x,y;0) = \sum_{m=0}^{m=\infty} \overline{A}_{0m}\sin\left(\frac{\mu_m y}{K}\right) = -\beta_y \frac{(T_a - T_0)}{1+\beta_y}\left(\frac{y}{L_2}\right) \tag{1.24}$$

This result confirms that the transient solution is independent of x, i.e. the temperature distribution is one dimensional and only depends on properties in the y or thickness direction.

From (1.10d), $\mu_m L_2/K$ are the roots of the equation

$$\frac{\mu_m L_2}{K}\cot\frac{\mu_m L_2}{K} + \beta_y = 0 \tag{1.25}$$

By multiplying both sides of (2.24) by $\sin(\mu_m y/K)$, integrating over the range $0<y<L_2$, and using $\lambda_m = \frac{\mu_m L_2}{K}$ result

$$\overline{A}_{0m} = 2\beta_y \frac{(T_a - T_0)[-\sin\lambda_m + \lambda_m\cos\lambda_m]}{(1+\beta_y)\lambda_m[\lambda_m - 0.5\sin 2\lambda_m]} \tag{1.26}$$

is obtained. The non-dimensional temperature distribution is then given by

$$\frac{T(y^*;t^*)}{T_a - T_o} = \frac{\beta_y}{1+\beta_y}\left\{y^* + 2\sum_{m=0}^{m=\infty}\frac{[-\sin\lambda_m + \lambda_m\cos\lambda_m]}{\lambda_m[\lambda_m - 0.5\sin 2\lambda_m]}\sin\lambda_m y^*\exp[-\lambda_m^2 t^*]\right\} \tag{1.27}$$

2.4.2 Stress Analysis

For the case of a plane thermoelastic problem being considered, the state of stress in the sample may be either a plane stress state (sample is very thin in the z direction) or a plane strain state (sample is very thick in the z direction). For the particular case studied, the sample may be considered to be in a plane strain state, although obtaining the plane stress results requires only a simple modification. For geometries where plane strain can be assumed, the stress components are given by

$$\begin{aligned}
\sigma_{xx}(x,y;t) &= A_{11}\frac{\partial u}{\partial x} + A_{12}\frac{\partial v}{\partial y} - \beta_1 T(x,y;t)\\
\sigma_{yy}(x,y;t) &= A_{21}\frac{\partial u}{\partial x} + A_{22}\frac{\partial v}{\partial y} - \beta_2 T(x,y;t)\\
\sigma_{zz}(x,y;t) &= A_{31}\frac{\partial u}{\partial x} + A_{32}\frac{\partial v}{\partial y} - \beta_3 T(x,y;t)\\
\sigma_{xy} &= A_{44}\left(\frac{\partial u}{\partial y} + \frac{\partial v}{\partial x}\right)
\end{aligned} \tag{2.1}$$

where the A_{ij} are the stiffness coefficients for the orthotropic material and β_{ij} are the stress-temperature coefficients. The displacement form of the equilibrium equations then is

$$A_{11}\frac{\partial^2 u}{\partial x^2} + A_{44}\frac{\partial^2 u}{\partial y^2} + (A_{12} + A_{44})\frac{\partial^2 v}{\partial x \partial y} = \beta_1 \frac{\partial T}{\partial t}$$

$$A_{22}\frac{\partial^2 v}{\partial y^2} + A_{44}\frac{\partial^2 v}{\partial x^2} + (A_{32} + A_{44})\frac{\partial^2 u}{\partial x \partial y} = \beta_2 \frac{\partial T}{\partial t} \qquad (2.2)$$

For the one-dimensional case being considered here, there should be no x dependence of the stress components. Assuming a stress free state on the surfaces y=0, L_2 the equilibrium equations, together with a consideration of force and moment equilibrium across the sample, as shown for example in Boley and Weiner (1960), give the solutions

$$\sigma_{xx} = \left(\frac{A_{12}\beta_2}{A_{22}} - \beta_1\right)\left\{T - \left(\frac{4L_2 - 6y}{L_2^2}\right)\int_0^{L_2} T dy - \left(\frac{12y - 6L_2}{L_2^3}\right)\int_0^{L_2} Ty\ dy\right\}$$

$$\sigma_{yy} = \sigma_{xy} = 0$$

$$\sigma_{zz} = \left(\frac{A_{32}\beta_2}{A_{22}} - \beta_3\right)\left\{T - \left(\frac{4L_2 - 6y}{L_2^2}\right)\int_0^{L_2} T dy - \left(\frac{12y - 6L_2}{L_2^3}\right)\int_0^{L_2} Ty\ dy\right\} \qquad (2.3)$$

It is clear from (2.3) that if the temperature is linear in the y direction then the stress is everywhere zero. Therefore, with either a zero temperature boundary condition on the y=0 surface, which leads to a linear steady-state temperature distribution, or the zero flux boundary condition on the y=0 surface, which leads to a uniform steady-state temperature distribution, the steady-state stress will be zero. However, the stress distribution will vary considerably through the transient.

Substituting the temperature distribution from (1.28) into (2.3), it is found that a non-dimensional form of the stress component σ_{xx} is

$$\frac{\sigma_{xx}(y^*;t)}{E_x\alpha_x(T_a - T_o)} = 2\left(\frac{A_{12}\beta_2}{A_{22}} - \beta_1\right)\frac{\beta_y}{1 + \beta_y}$$

$$\sum_{m=0}^{m=\infty}\left\{\frac{[-\sin\lambda_m + \lambda_m\cos\lambda_m]}{\lambda_m[\lambda_m - 0.5\sin 2\lambda_m]}\left[\sin\lambda_m y^* - \frac{(2-6y^*)}{\lambda_m}\cos\lambda_m - \frac{(4-6y^*)}{\lambda_m} - \frac{(12y^*-6)}{\lambda_m^2}\sin\lambda_m\right]\exp[-\lambda_m^2 t^*]\right\} \qquad (2.4)$$

for the constant temperature boundary condition on the bottom surface.

2.4.3 Analytic Results

The results given in this section are equally valid for either the shock-up condition ($T_a > T_o$) or a shock-down condition ($T_a < T_o$) since the temperature and stress distributions are normalized with respect to the factor $T_a - T_o$. For the purposes of presenting the results however, all graphs are given with respect to the shock-up case.

Figure 10 presents results from the program HEAT2D. This program is a two-dimensional finite element heat transfer code. HEAT2D was used to determine temperature distributions for the two-dimensional thermal problem described in Section 4.1. The Biot number was taken to be 1.0, and the Fourier number was 0.1. The temperature is plotted as a function of distance along the x, or fiber, direction. Only half the plate has been plotted since the problem is symmetrical. The temperature is plotted at a constant value of y/L_2, and it is clearly seen that away from the extreme edges of the sample, the temperature distribution can be considered one-dimensional.

In Table 2, a comparison is made between temperature calculated using the closed form solution described in Section 4.1 and the temperatures calculated by HEAT2D, some of which are presented Figure 10. In each case, the temperatures are normalized, and the values tabulated are $(T-T_o)/(T-T_a)$. In Figure 10, the Biot number is 1.0 and the Fourier number is 0.1. It must be emphasized here that in order to calculate the temperatures from the finite element code HEAT2D, a transient analysis had to be performed, which is time consuming. With the direct calculation, no iteration is required, the result may be obtained directly for any value of time. Also, the temperature and stress at any location may be calculated instead of interpolating between grid points in the finite element method.

Figure 11 presents the temperature distribution and corresponding stress distribution (in the x, or fiber, direction) induced through the thickness of the plate for a Biot number of 1.0. The stress plots are presented such that the solid lines correspond to times leading up to the peak transient stress and dashed lines correspond to times following peak transient stress.

The greatest magnitude of stress is found on the upper surface, although this stress is tensile only for the shock-down condition. In the case of the shock-up condition, peak tensile stress is located inside the plate. Figure 12 shows the temperature distribution and corresponding upper surface stress as a function of time. The stress plot shows how the time at which peak stress is attained is a function of the Biot number (or equvalently of the heat transfer coefficient at the upper surface). If the Biot number becomes very large (or as the shock conditions become more severe) the thermal shock instantaneously produces the peak stress. Using Figure 12 it is possible to use experimental values of temperature at various times and positions to back-calculate the magnitude of the Biot number and thus the heat transfer coefficient for the experiment.

An important consideration in this analysis was to begin to formulate a failure criterion for the CMC under thermal shock conditions. For the purposes of the current analysis, failure was considered to occur when the stress on the upper surface exceeds the strength of the material, as determined from mechanical testing. For different values of the Biot number, the maximum normalized stress, $\sigma_{xx}/E_x\alpha_x(T_a-T_o)$, may be determined. From this, the temperature change (T_a-T_o) needed to produce failure may be calculated. Only the shock-down case is considered here, since the shock-up case leads to compressive stress on the upper surface. Tables 3 and 4 show the maximum stress produced for various values of the Biot number and the temperature change required to produce failure. It is clear from Tables 3 and 4 that if exceeding the material strength on the surface of the plate is the failure mechanism, then the sample will fail in the transverse direction, i.e. parallel to the fibers.

2.4.4 Parametric Study

As noted previously, the temperature and stress distributions calculated are independent of x. The only material parameter the temperature distribution depends on is the through thickness thermal conductivity, K_y. Figure 13 shows the effect of K_y on the temperature at the upper surface of the sample. K_y refers to the baseline conductivity measured for the material system. The heat transfer coefficient is held constant such that for the baseline conductivity the Biot number is unity. Thus, the only effect being considered is the change of conductivity. From Figure 13, it is clear that the upper surface temperature decreases with increasing thermal conductivity. As with temperature, the magnitude of peak surface stress also decreases with increasing thermal conductivity (Figure 14), since the rate of change in the thermal gradient is less severe through the transient.

For the one-dimensional case studied, the stress distribution is directly proportional to a function of temperature, as given in (3.3). The only involvement of the elastic constants occurs in the multiplying factor of this temperature function. For a state of plane strain, such as exists for the case studied, the stress in the fiber direction, σ_{xx}, and the stress in the transverse direction, σ_{zz}, can be expressed in the form

$$\frac{\sigma_{xx}}{E_x\alpha_x} = -\frac{\left(1 + \frac{E_z}{E_x}\frac{\alpha_z}{\alpha_x}\nu_{xz}\right)}{1 - \frac{E_z}{E_x}\nu_{xz}^2} f(T) \quad \text{and} \quad \frac{\sigma_{zz}}{E_x\alpha_x} = -\frac{\frac{E_z}{E_x}\left(\frac{\alpha_z}{\alpha_x} + \nu_{xz}\right)}{1 - \frac{E_z}{E_x}\nu_{xz}^2} f(T) \tag{4.1}$$

It is a simple matter to determine how the stress will change as E_z/E_x, ν_{xz}, and α_z/α_x change. It is clear from (4.1) that if $E_z\nu_{xz}^2$ is small compared to E_x, then the relationship between the normalized stress and E_z/E_x, ν_{xz}, and α_z/α_x is virtually linear. Table 5 gives the value of the factors that multiply the temperature functions for a range of E_z/E_x ratios. The baseline case has a modulus ratio of ~0.025.

It is clear that both stress components are monotonically increasing functions of the modulus ratio, the thermal expansion ratio, and Poissons's ratio. However, the resultant increase in stress must be weighed against changes to material strength. It has been observed that while modulus, thermal expansion coefficient, and Poisson's ratio, and thus thermal stress, increase linearly with decreasing porosity, the strength increases exponentially. Thus, decreasing porosity, and increasing modulus, thermal expansion coefficient, and Poisson's ratio, as well as strength, could have significant benefit.

3.0 Experimental Results

3.1 Baseline Material Properties

In general, the mechanical testing showed the two composites to have good in-plane, fiber dominated properties while matrix dominated properties, such as interlaminar shear, [90] tension,etc., were quite low. The low matrix dominated properties made testing difficult-to-impossible for some of the desired properties. In particular, the [90] properties in tension and compression were impossible to determine due to specimen failure during installation into the test frame. Also, the interlaminar fracture toughness of the two systems could not be measured, as the interlaminar strengths of both composite systems were small. The determination of the interlaminar properties themselves, as well as [0] compressive behavior, was quite difficult.

The thermal conductivity of the two systems was determined from thermal diffusivity measurements, using the laser flash method, mass density, and specific heat measurements. Thermal expansion was determined through expansion testing to 1200 C with a quartz dilatometer.

The properties obtained for the two systems are summarized in Table 6. Strength values shown are ultimates and modulii are initial tangent values. From this data several observations may be made. First, there was a significant increase in the compressive strength with increasing temperature for the two CMC systems. This increase would not appear to be due to improved fiber strength, as tensile strength was observed to decrease with temperature. Additionally, matrix properties did not appear to improve with increasing temperature based upon the interlaminar shear strength. Second, as was expected, the thermal conductivity of the two CMC's was very low; however, there was a bit more anisotropy in thermal conductivity than was expected, particularly for the sapphire reinforced system. Additional observations may be made concerning the general response of the material. From the tensile stress-strain response (Figure 15), no obvious matrix cracking stress can be seen, even though it is known that the matrix cracks at strains of ~0.05% from surface replication and matrix testing conducted by GEAE under IR&D. From this, it may be concluded that matrix fracture has little effect on the stress-strain response or fracture of the composite.

3.2 Thermal Shock Properties

The test plan for thermal shock evaluation is shown in Table 7. Since the samples were unidirectional, the low matrix dominated properties resulted in failure of some samples during both the pre- or post-shock machining operation. Post-shock evaluation included optical inspection of the sample surface exposed to the shock, compression and interlaminar shear testing of shocked material, and microstructural evaluation of shocked material. Optical inspection, at a magnification of ~ x25, revealed some indications of transverse failure; however, these indications were not consistent and could not be related to shock severity. Examples of surface indications for shocked samples are shown in Figures 16 and 17 for the Sumitomo and sapphire systems, respectively.

Mechanical testing of the shocked material was limited to determining compressive and interlaminar shear strength, as these two properties were considered to be most sensitive to the matrix damage observed in the shocked samples. The selection of these two properties should also give some estimate of depth of damage in the composite systems since the interlaminar shear measurements were expected to be insensitive to surface damage while compressive strength should be sensitive to damage through out the sample.

Results of post-shock compression testing on the Sumitomo and sapphire systems are shown in Figures 18 and 19, respectively. From these results, it is seen that for the moderate shock-down condition, the compressive properties of both the Sumitomo and sapphire systems are unaffected. This suggests that the matrix damage is minimal for these conditions. For the severe shock-down and the moderate and severe shock-up conditions, significant decrease in compressive strength, up to 50% reduction, was observed. In the case of the severe shock-down conditions, some dependence of compressive strength knock-down on shock cycles was observed. This suggests some accumulation of matrix damage due to repeated shock exposure; however, the matrix damage appears to saturate after ~10-20 shock cycles. The results of the interlaminar shear testing are inconclusive. The strengths obtained from post-shock testing showed no trend, perhaps suggesting that no damage was occuring in the interior of the test samples. This was surprising since the shock-up test results showed significant decreases in compressive strength, which were associated with interior damage (the location of highest tensile stress). Based upon this information, it was concluded that all matrix damage was isolated to the exterior of the samples.

Post-shock testing on the planar shock samples showed no degradation in either the compressive strength or the interlaminar shear strength. This was likely due to a combination of the mild thermal shock conditions for this configuration and the orientation of the fiber direction to the thermal gradient. However, the thermal gradients experienced by the test samples were on the order of gradients anticipated during "hot streaks" in engine operation.

The post-shock microstructural evaluation showed that indeed the matrix damage was isolated to the exterior of the samples. Figure 20 shows the surface of a typical Sumitomo reinforced specimen, subjected to a "severe" shock-down condition for 10 cycles. From this photomicrograph it is apparent that the matrix cracking originates at the surface of the sample and terminates several plies into the specimen. The nature of this matrix microcracking is such that the matrix appears to "crumble" resulting in localized spallation of the matrix. The severity of the thermal shock appears to control the severity of the matrix microcracking. In moderate thermal shocks, the microcracking remained sparse and did not result in matrix spallation. In the severe shock cases the microcracking appeared to be dense leading to the crumbling and spallation of the matrix. This agrees well with the analytic results and confirms conclusions made upon completion of mechanical testing of shocked material. Post-shock microstructural evaluation of the Sapphire reinforced material showed that damage was not as severe as with the Sumitomo system. Some microcracking was observed for the Sapphire material but no crumbling or spallation was observed.

4.0 Conclusions and Recommendations

Some insights into the thermal shock behavior of fiber reinforced ceramics can be made from the results of this program. First, the predominant failure mode observed was surface originating matrix fracture. Analysis suggests that this failure mode would dominate even at very severe shock conditions. Second, the effect of this matrix failure is isolated to reductions in matrix dominated properties such as the compressive strength and [90] tensile strength for the two oxide-based CMC's evaluated under this program. While interlaminar properties are dominated by matrix performance, the localization of matrix damage to the surfaces of the material, even after repeated shocks, results in little-to-no effect on interlaminar properties. Additionally, the direction of crack propagation was observed to be perpendicular to the laminae interfaces; therefore, little influence of matrix damage on the interlaminar shear and tensile strength would be anticipated. It must be noted that the thermal shock behavior of the CMC systems evaluated in this program is highly dependent upon the failure process. The failure process of the Sumitomo and sapphire reinforced systems is dominated by fiber fracture with matrix fracture playing an insignificant role in ultimate failure of the composite system. This is not the case for other composite systems, such as SiC/SiC and dense alumina matrix composites. In these composites matrix fracture plays a significant role in the ultimate failure process; therefore, the thermal shock induced matrix damage may have a significant effect even on fiber-dominated properties such as tensile strength.

A simplified model of the thermal shock behavior of unidirectionally reinforced ceramic composites was developed. This model assisted in gaining greater insight into the thermal shock behavior for the CMC' s of interest in this study. Perhaps the most important observation made from the analysis was the required magnitude of the thermal shock severity required to induce fiber fracture. Additional understanding of the influence of microstructure on thermal shock behavior was obtained by evaluating the effects of elastic properties on thermal shock response. From this parametric analysis it was seen that the stress state is linearly dependent on the elastic properties of the composite, and further, dependence on microstructural features such as porosity was also linear. However, the dependence of strength on porosity has been observed to be exponential; thus while the transient stress state may be relatively unaffected by changes in porosity the strength, and thus ultimate fracture, may be significantly affected by a decrease in porosity.

This first look at the thermal shock resistance of CMC's provided significant understanding of the failure mechanisms associated with thermal shock and the material properties which most influence thermal shock response. Even so, significant issues remain unanswered. In particular, the understanding of how microstructure influences thermal shock behavior is at best qualitative. Significant effort will be required to provide a mechanistic understanding. Additionally, the evaluation of unidirectional composites may have skewed the perspective of thermal shock response. Examination of multidirectional reinforced CMC's may show that thermal and mechanical anisotropy of the system gives rise to significant interlaminar stresses which will alter the fracture process observed for the unidirectional composites.

To grasp a full understanding of the influence of constituent properties and microstructure on the thermal shock resistance of ceramic composites, more detailed analysis should be performed extending the level of datail down to the microstructural level. Thus, the material scientist may observe the interplay of various material parameters on the thermal shock behavior of the system. This may be readily performed by extending the parametric study presented in this program to include micromechanics descriptions of the elastic properties making up the thermal stress equation.

While extension of the material parametric studies will provide valuable insight into the thermal shock process and the influence of material properties on thermal shock performance, there must be further effort in describing the fracture process. The current study has assumed an orthotropic, homogeneous elastic medium to develop the thermal stress distributions during a thermal shock event. However, it is well known that the heterogeneous nature of ceramic composites is what provides the improved toughness of the composite relative to the monolithic ceramic. Effort in determining the appropriate failure criteria for the thermal shock problem, taking into account the heterogeneous nature of the material system, would be beneficial in assessing the suitability of ceramic composites for utilization in specific applications.

5.0 References

1) A.Y. Akoz and T.R. Tauchert, "Thermomechanical Analysis of a Finite Orthotropic Slab", J. Mech. Eng. Sci. 20, pp 65-71 (1978)

2) H.S. Wang and T.W. Chou, "Transient Thermal Stress Analysis of a Rectangular Orthotropic Slab", J. Comp. Mat. 19, pp 424-441 (1985)

3) H.S. Wang and T.W. Chou, "Transient Thermal Behavior of a Thermally and Elastically Orthotropic Medium", AIAA 24, pp 664-672 (1986)

4) B.A Boley and J.H. Weiner, Theory of Thermal Stresses, John Wiley, New York, (1960)

Table 1

Material Properties Used in Analysis

E_x	79.2 MPa
E_y	2.0 MPa
E_z	2.0 MPa
ν_{xz}	0.22
G_{xz}	4.0 MPa
K_x	2.0 W/m•K
K_z	0.55 W/m•K
α_x	5.9×10^{-6}/C
α_z	3.8×10^{-6}/C

Table 2

Comparison of Closed Form and Finite Element Temperature Solutions

y/L_2	Direct Calculation Temperature	Finite Element Temperature
0.125	5.873E-3	6.188E-3
0.250	1.419E-2	1.460E-2
0.375	2.766E-2	2.777E-2
0.500	4.932E-2	4.970E-2
0.625	8.246E-2	8.078E-2
0.750	1.301E-1	1.274E-1
0.875	1.944E-1	1.913E-1
1.000	2.759E-1	2.734E-1

Table 3

Temperature Difference Required to Reach
"Breaking Stress" in the Fiber Direction

β	$\sigma_{xx}/E_x\alpha_x(T_a-T_o)$	T_a-T_o
0.5	0.046	24059
1.0	0.085	13020
5.0	0.266	4161
10.0	0.379	2920
20.0	0.497	2227
100.0	0.729	1518

Table 4

Temperature Difference Required to Reach
"Breaking Stress" in the Transvers Direction

β	$\sigma_{xx}/E_x\alpha_x(T_a-T_o)$	T_a-T_o
0.5	0.062	1281
1.0	0.113	703
5.0	0.356	223
10.0	0.508	156
20.0	0.666	119
100.0	0.976	81

Table 5

Variation of Stress Factors with Modulii Ratio

E_z/E_x	σ_{xx} Factors	σ_{zz} Factors
0.025	1.0047	0.0214
0.1	1.0189	0.0861
0.2	1.0381	0.1730
0.3	1.0574	0.2607
0.4	1.0769	0.3493
0.5	1.0965	0.4388
0.6	1.1164	0.5292
0.7	1.1365	0.6205
0.8	1.1568	0.7127
0.9	1.1773	0.8058
1.0	1.1980	0.8999

Table 6

Mechanical and Thermal Properties of
Sumitomo and Sapphire Reinforced Aluminosilicate

Sumitomo/Aluminosilicate

Property	Temperature (C)			
	20	900	1100	1300
[0] Tensile Modulus (msi)	11.27	11.18	11.52	
[0] Tensile Strength (ksi)	32.97	19.33	19.11	
[90] Tensile Modulus (msi)	----	----	----	
[90] Tensile Strength (ksi)	----	----	----	
[0] Compressive Modulus (msi)	11.25	5.85	5.66	
[0] Compressive Strength (ksi)	11.18	13.95	18.10	
[90] Compressive Modulus (msi)	----	0.09	----	
[90] Compressive Strength (ksi)	----	2.65	----	
In-Plane Shear Modulus (msi)	0.57			
In-Plane Shear Strength (ksi)	1.35			
Interlaminar Shear Str. (ksi)	0.34	0.38	0.10	
Interlaminar Tensile Str. (ksi)	0.04			
[0] CTE (in/in/°C)	2.0			
[90] CTE (in/in/°C)	1.67			
[0] Thermal Conductivity W/mK	2.17	2.03	2.08	
[90] Thermal Conductivity W/mK	0.83	0.85	1.03	

Sapphire/Aluminosilicate

Property	Temperature (C)			
	20	900	1100	1300
[0] Tensile Modulus (msi)	17.97		20.43	14.81
[0] Tensile Strength (ksi)	16.75		10.96	11.94
[0] Compressive Modulus (msi)	17.78			12.10
[0] Compressive Strength (ksi)	48.42			25.93
In-Plane Shear Strength (ksi)	6.21			
Interlaminar Shear Str. (ksi)	1.42			1.11
Interlaminar Tensile Str. (ksi)	0.08			
[0] CTE (in/in/°C)	2.50			
[90] CTE (in/in/°C)	----			
[0] Thermal Conductivity W/mK	11.08	4.38	4.49	4.57
[90] Thermal Conductivity W/mK	2.00	1.41	1.44	1.41

Table 7

Thermal Shock Test Plan

CMC System	Test Type	Cycles			
		1	10	100	1000
Sumitomo	Shock up-Moderate	1	1	2	2
	-Severe	2	2	2	
	Shock down-Moderate	1	1	2	2
	-Severe	2	2	2	
	In-plane-Moderate	1	1	2	2
	-Severe	2	2	2	
Sapphire	Shock up-Moderate		1	2	1
	-Severe	1	1	2	
	Shock down-Moderate		1	1	1
	-Severe	1	1	2	
	In-plane-Severe	1	1	1	

Figure 1

Fabrication Process for Aluminosilicate Composites

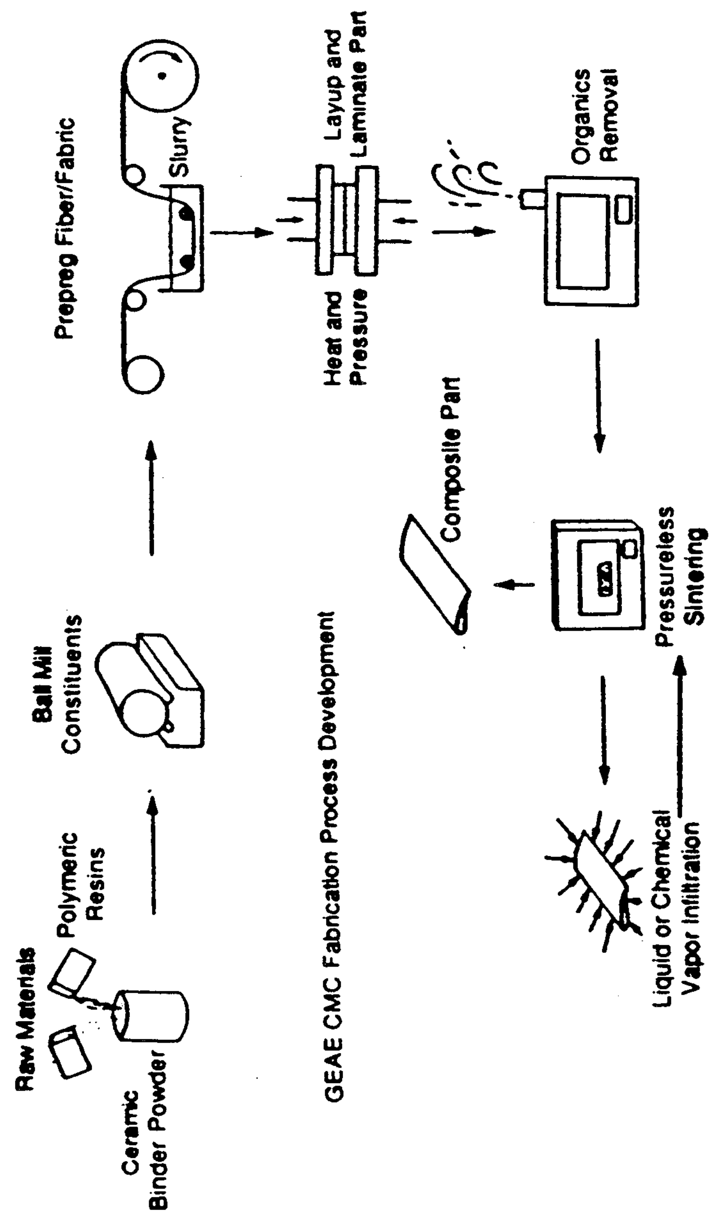

Figure 2

Test System Configuration for
Tensile Testing of Ceramic Composites

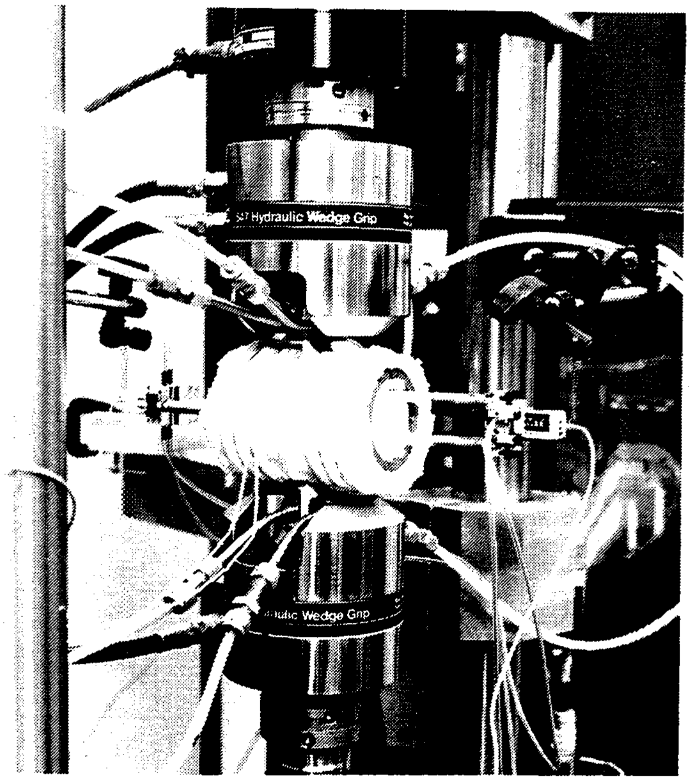

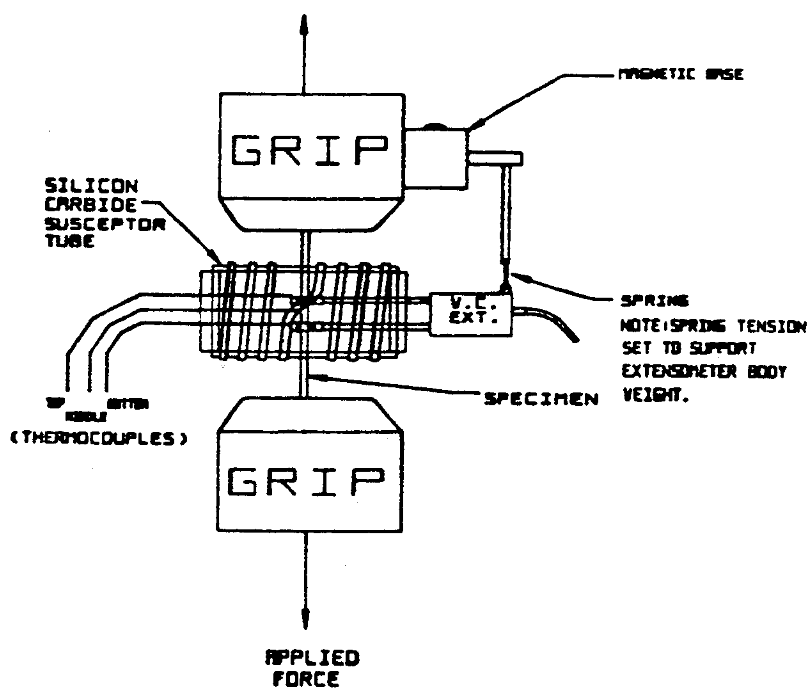

Figure 3

a) Conventional ASTM D695 Compression Fixture

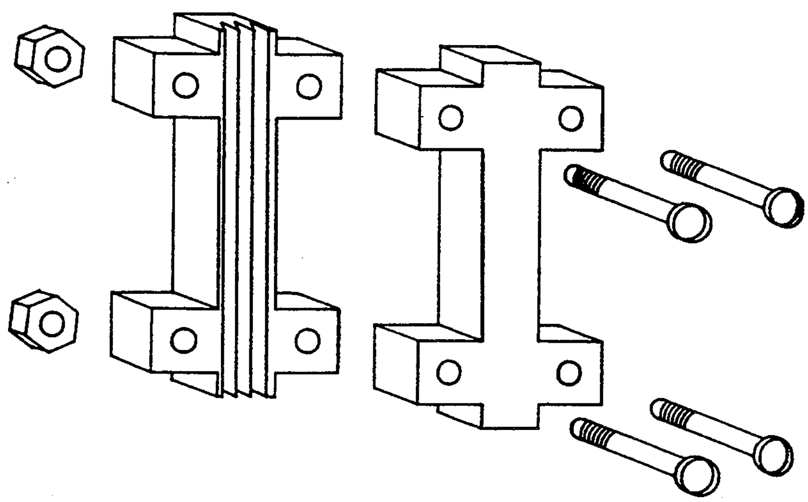

b) GEAE Modified Compression Fixture

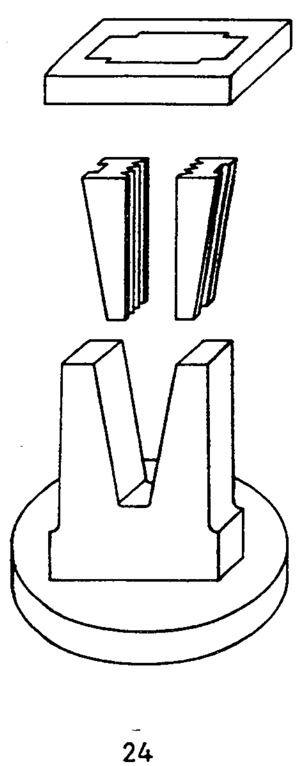

Figure 4

Double Notch Shear Specimen
for Interlaminar Shear Strength Determination

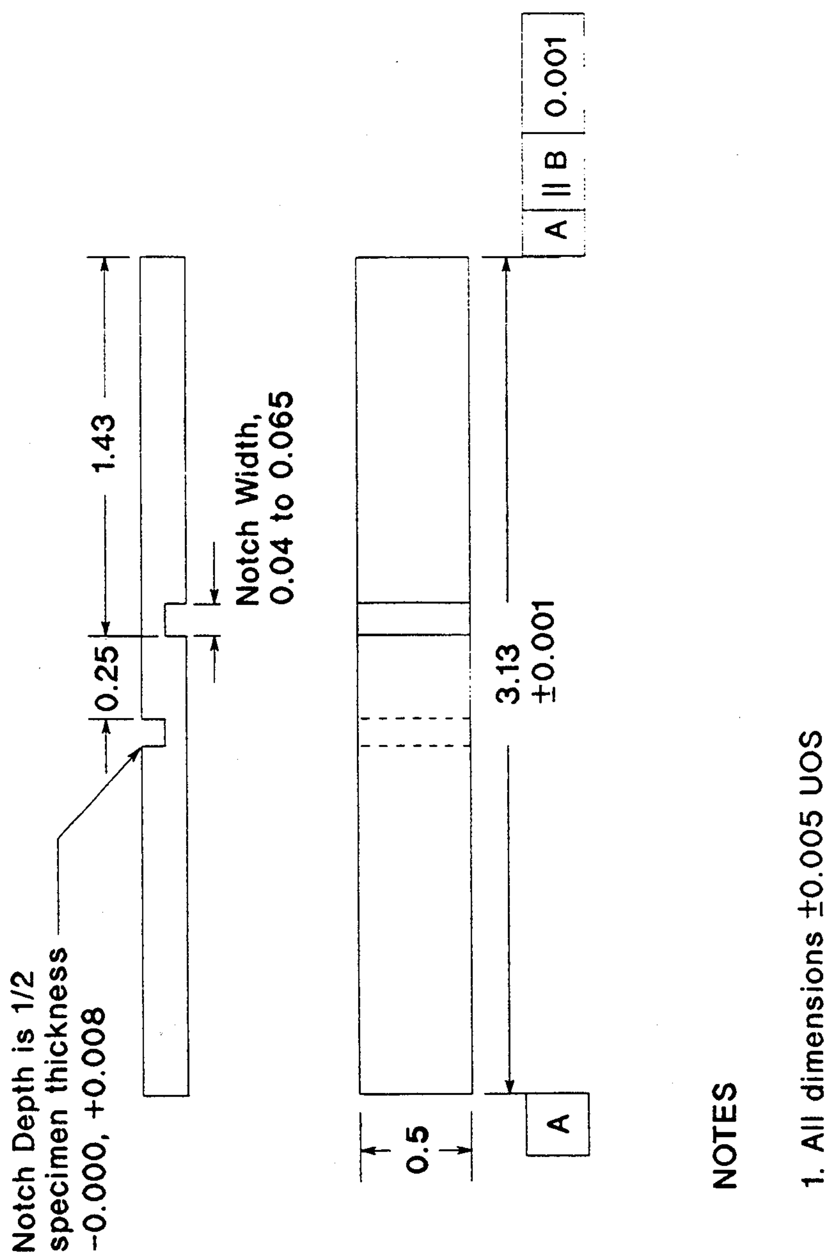

Ti 6-4 Tab

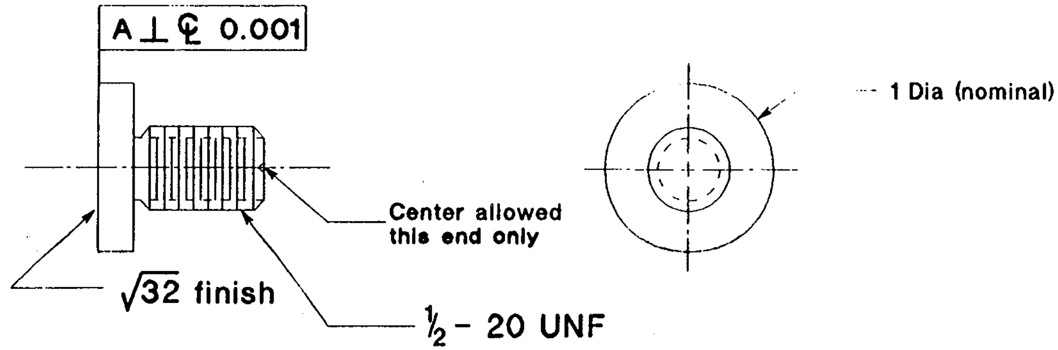

Specimen Assembly

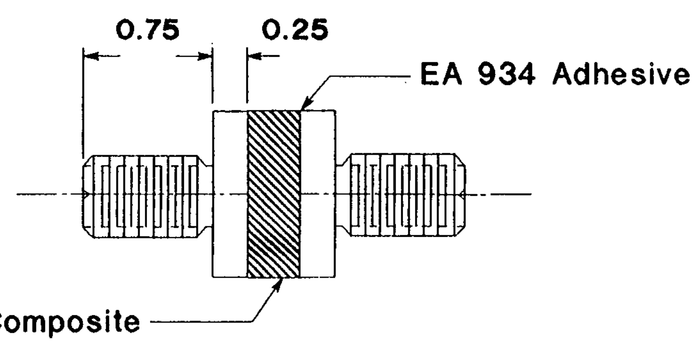

NOTES

1. All dia to be concentric to 0.001.

2. Finished assembly to be machined to remove adhesive flash.

Figure 5

Interlaminar Tension Test Specimen

Figure 6

Shock-down Test Facility

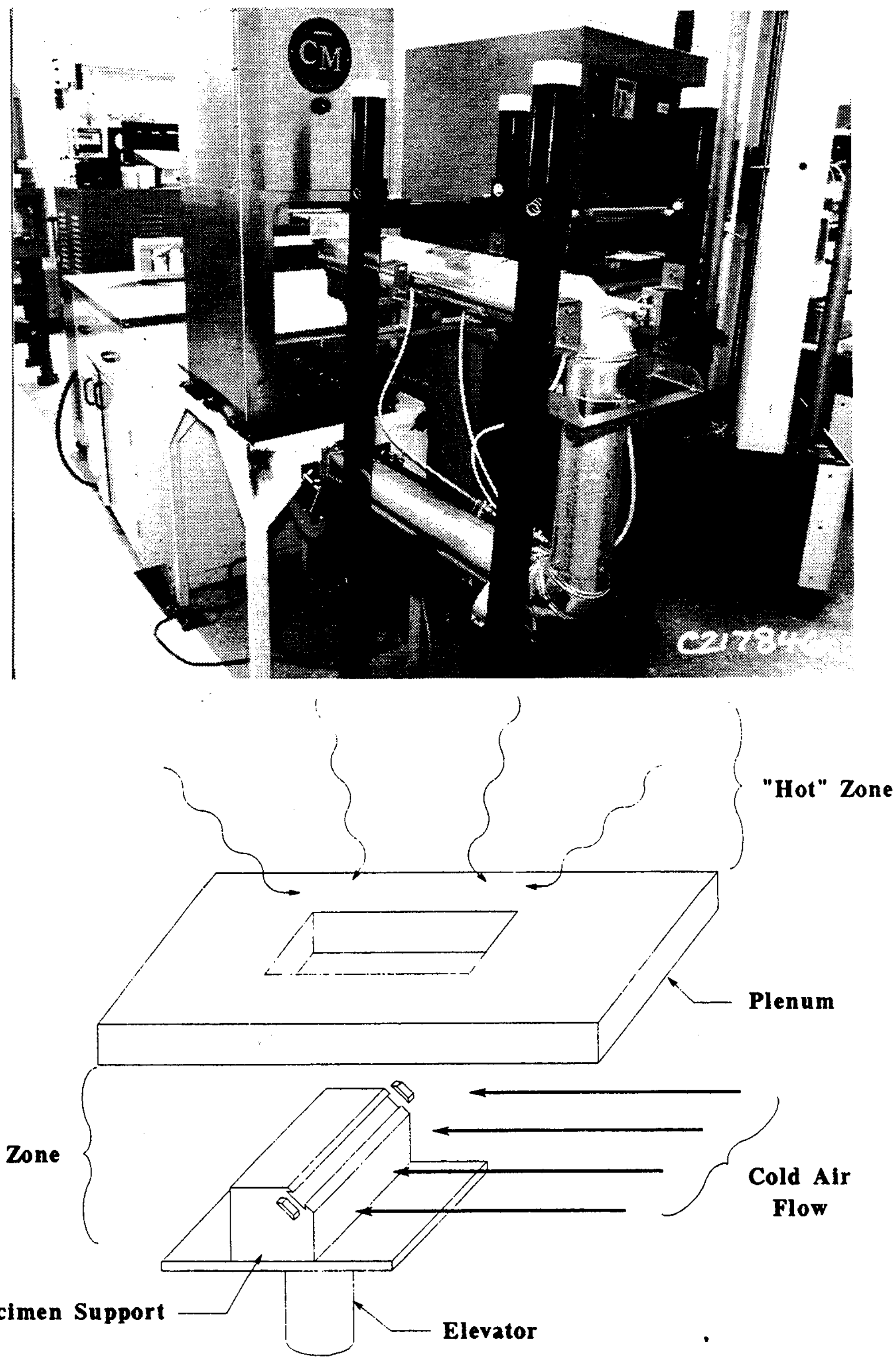

Figure 7

Shock-up Test Facility

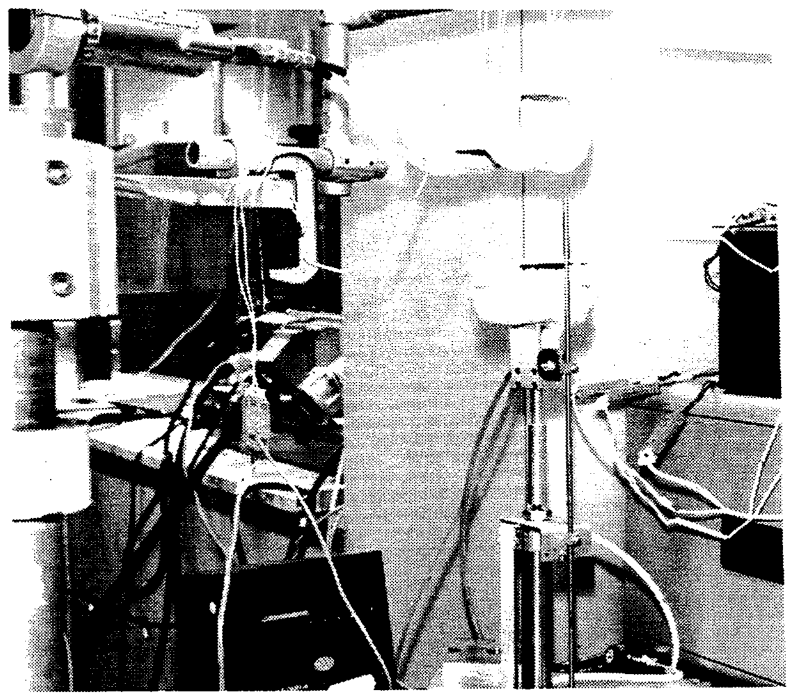

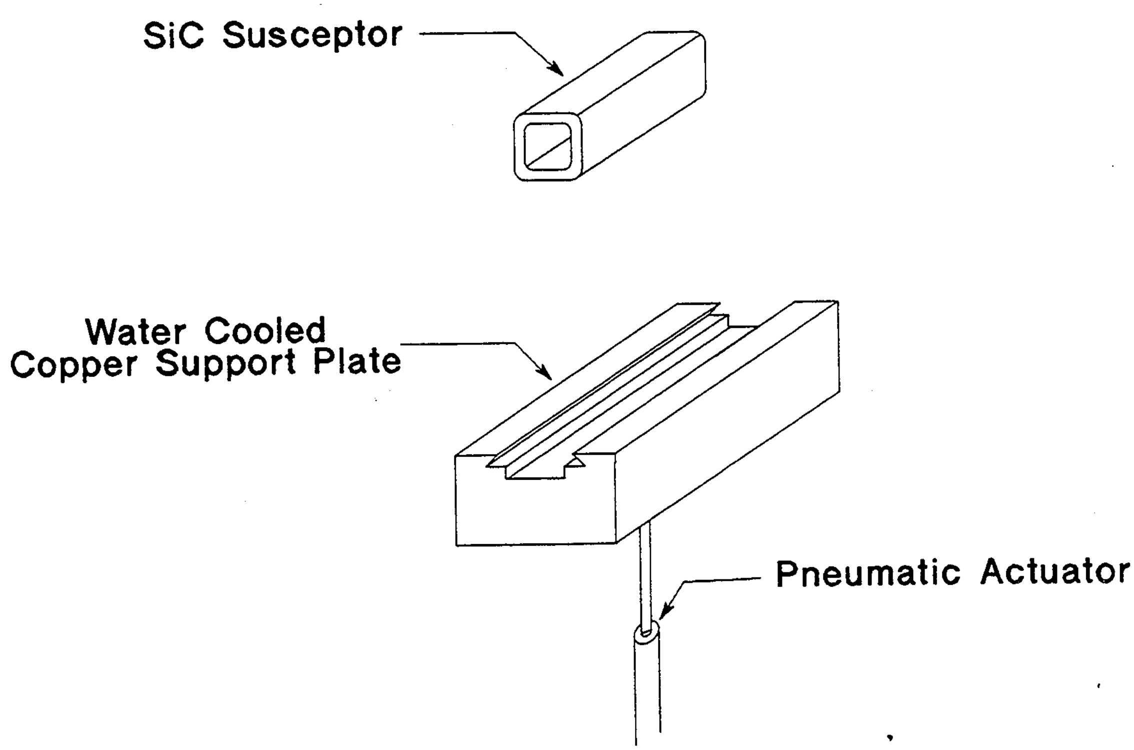

Figure 8

Planar Shock Test Facility

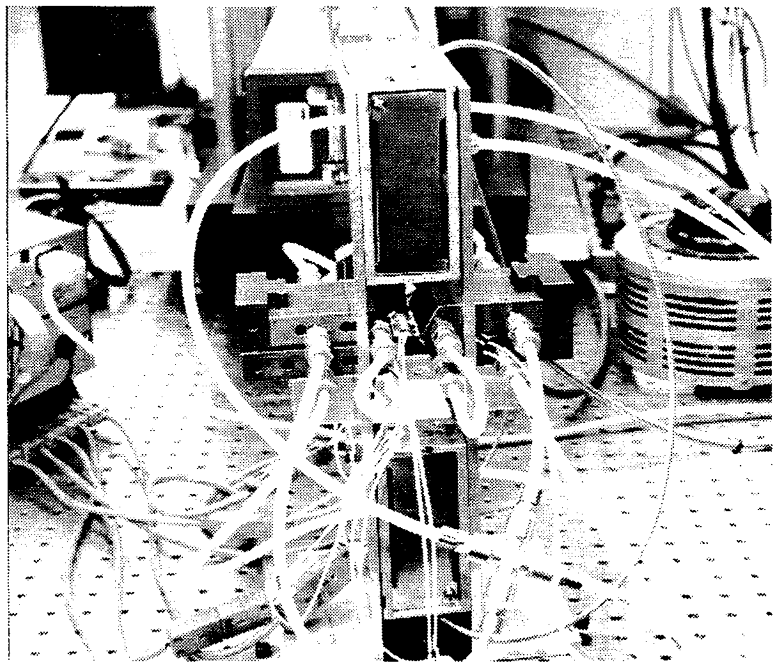

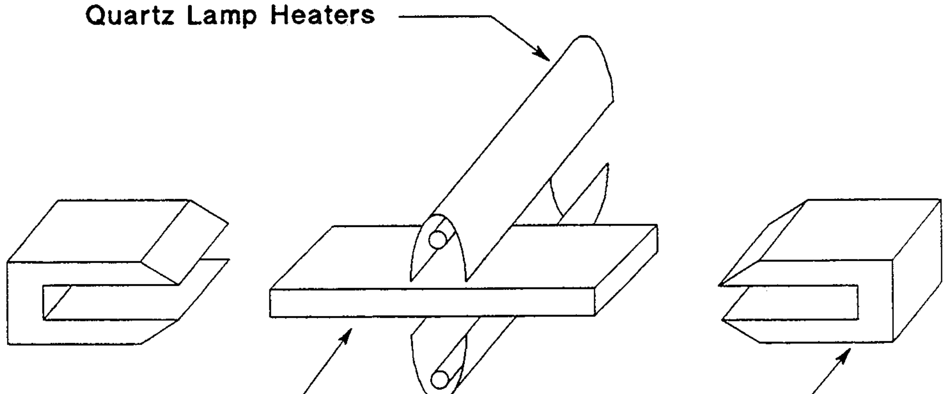

Figure 9

Plate Geometry for Thermal Shock Model

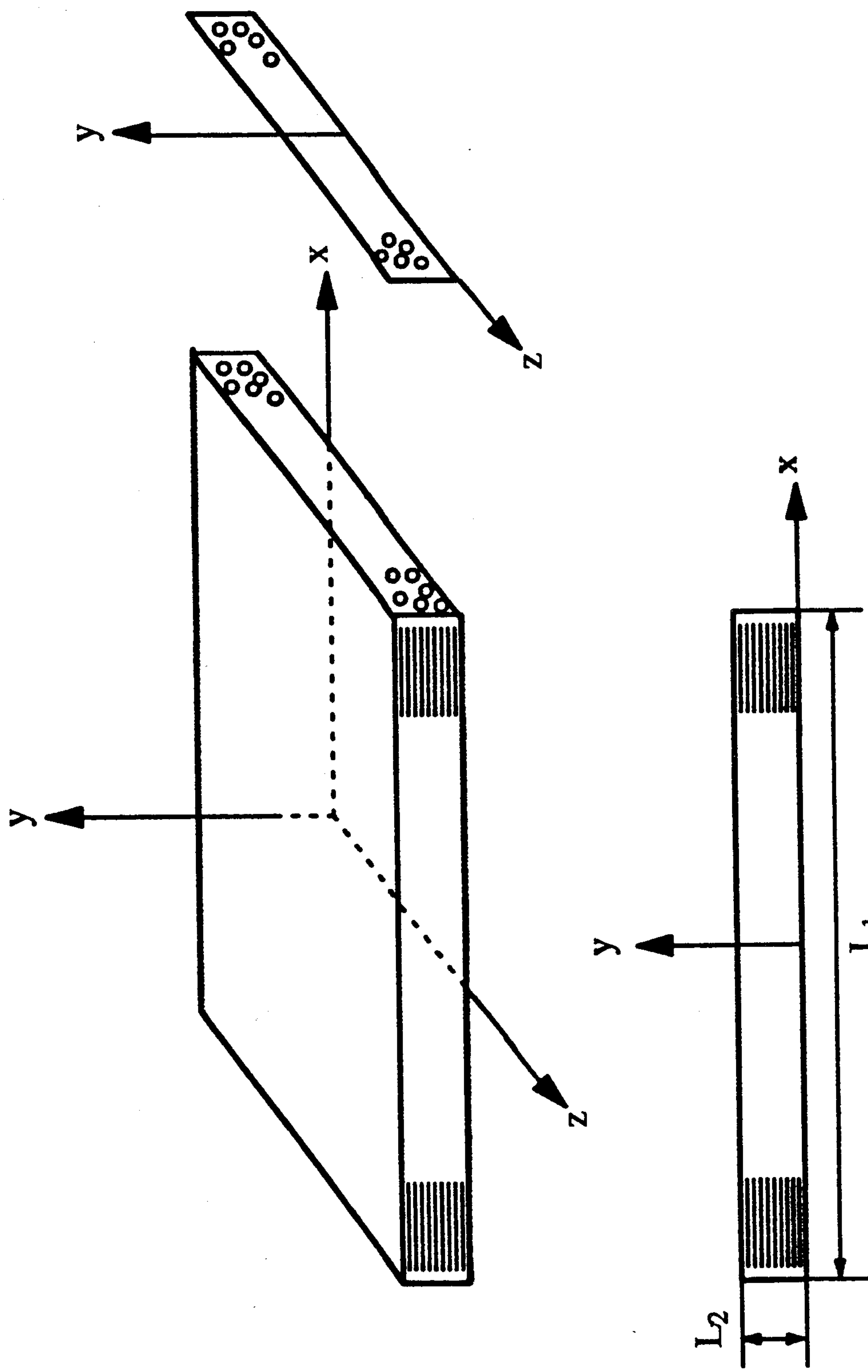

Figure 10

Temperature Distribution from HEAT2D

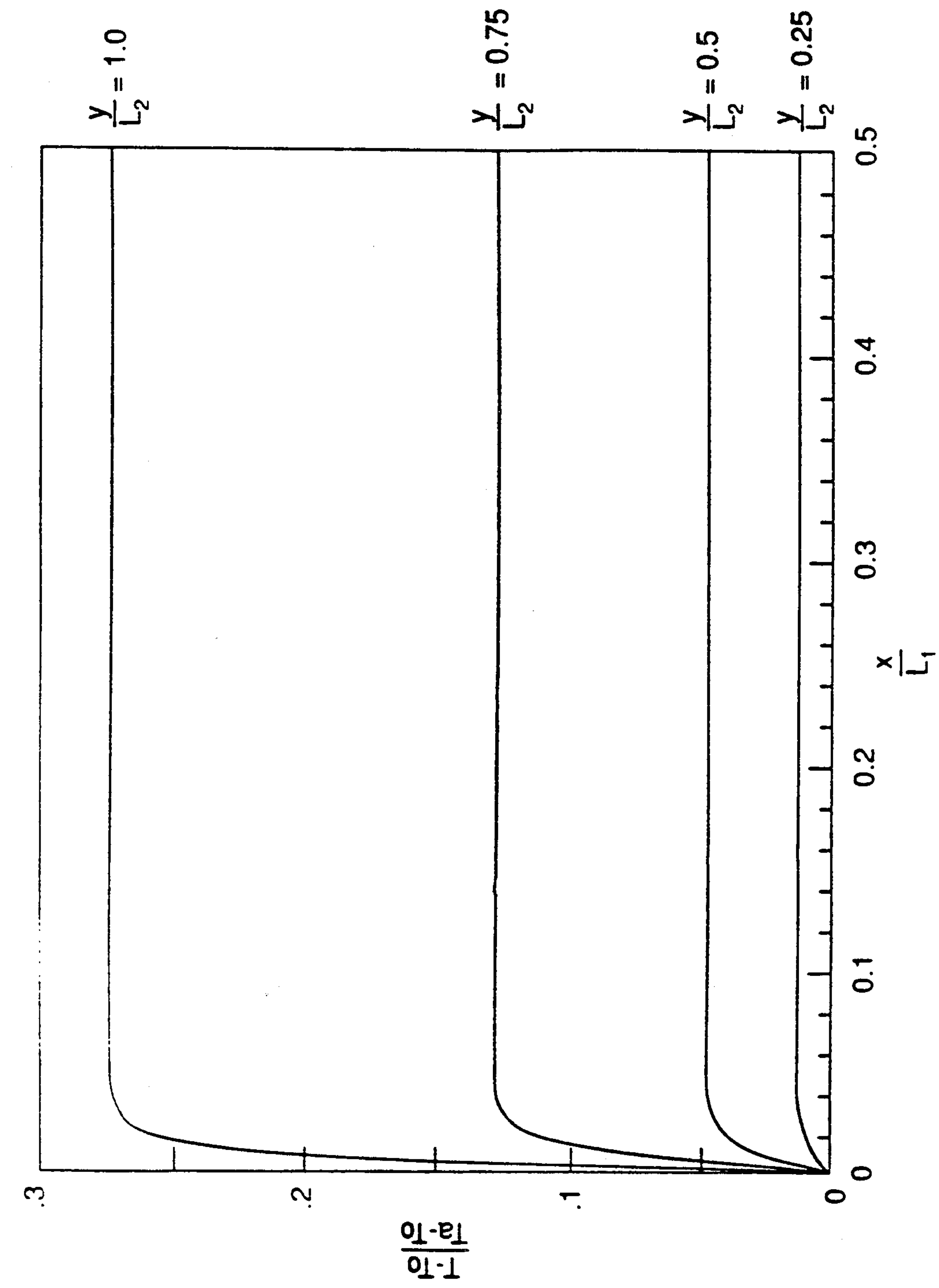

Figure 11

Transient Temperature and Stress Distribution for β=1.0

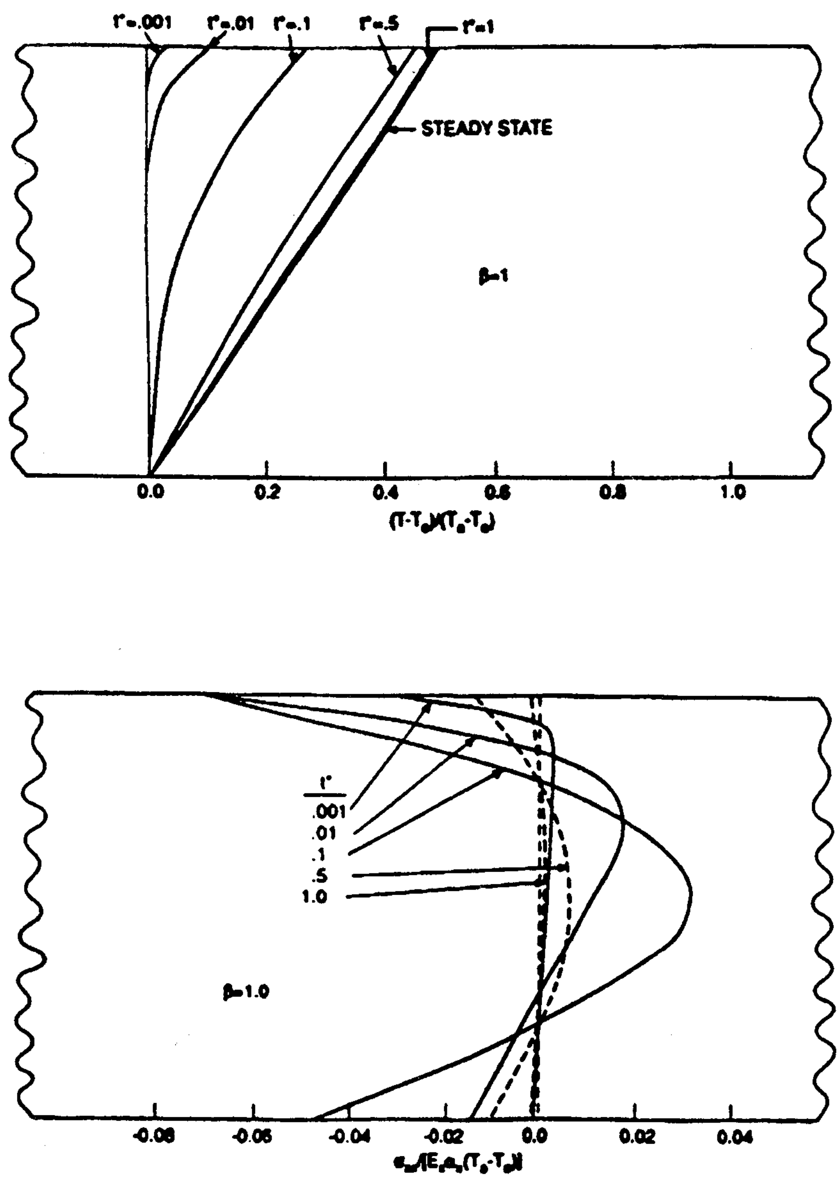

Figure 12

Transient Temperature and Stress Distribution
at Plate Surface for β=1.0

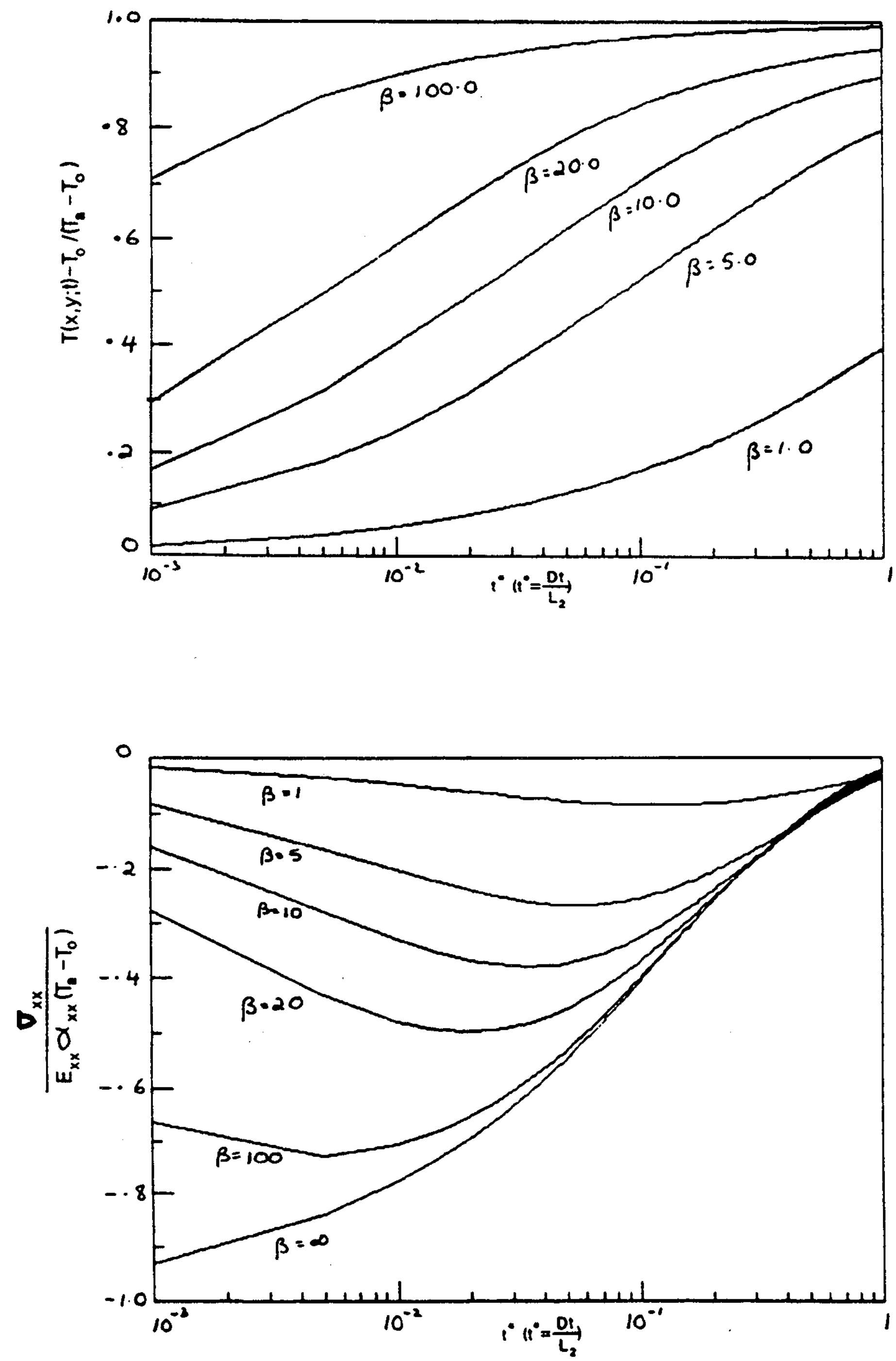

Figure 13

Effect of Thermal Conductivity on
Surface Temperature Distribution

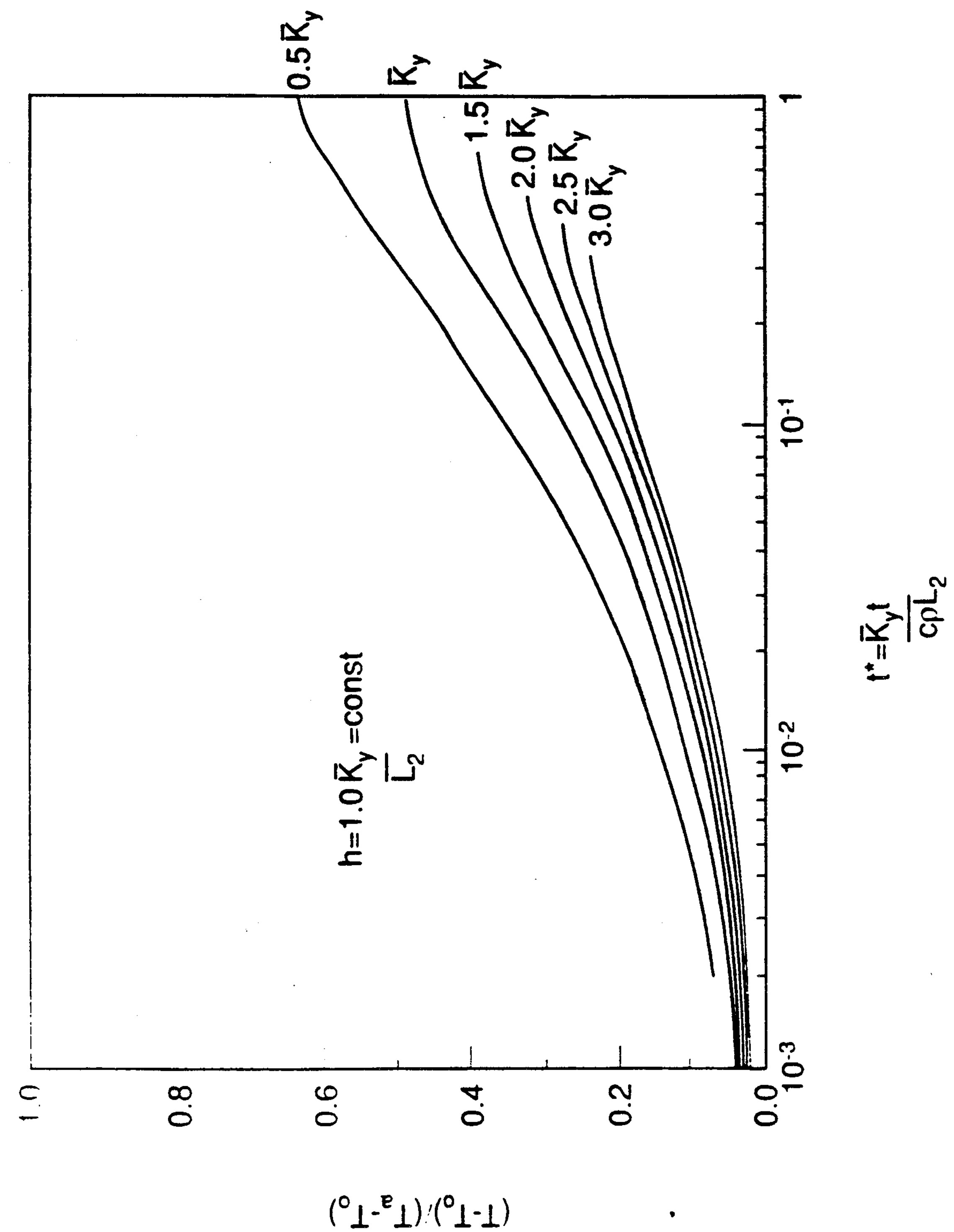

Figure 14

Effect of Thermal Conductivity on
Surface Stress Distribution

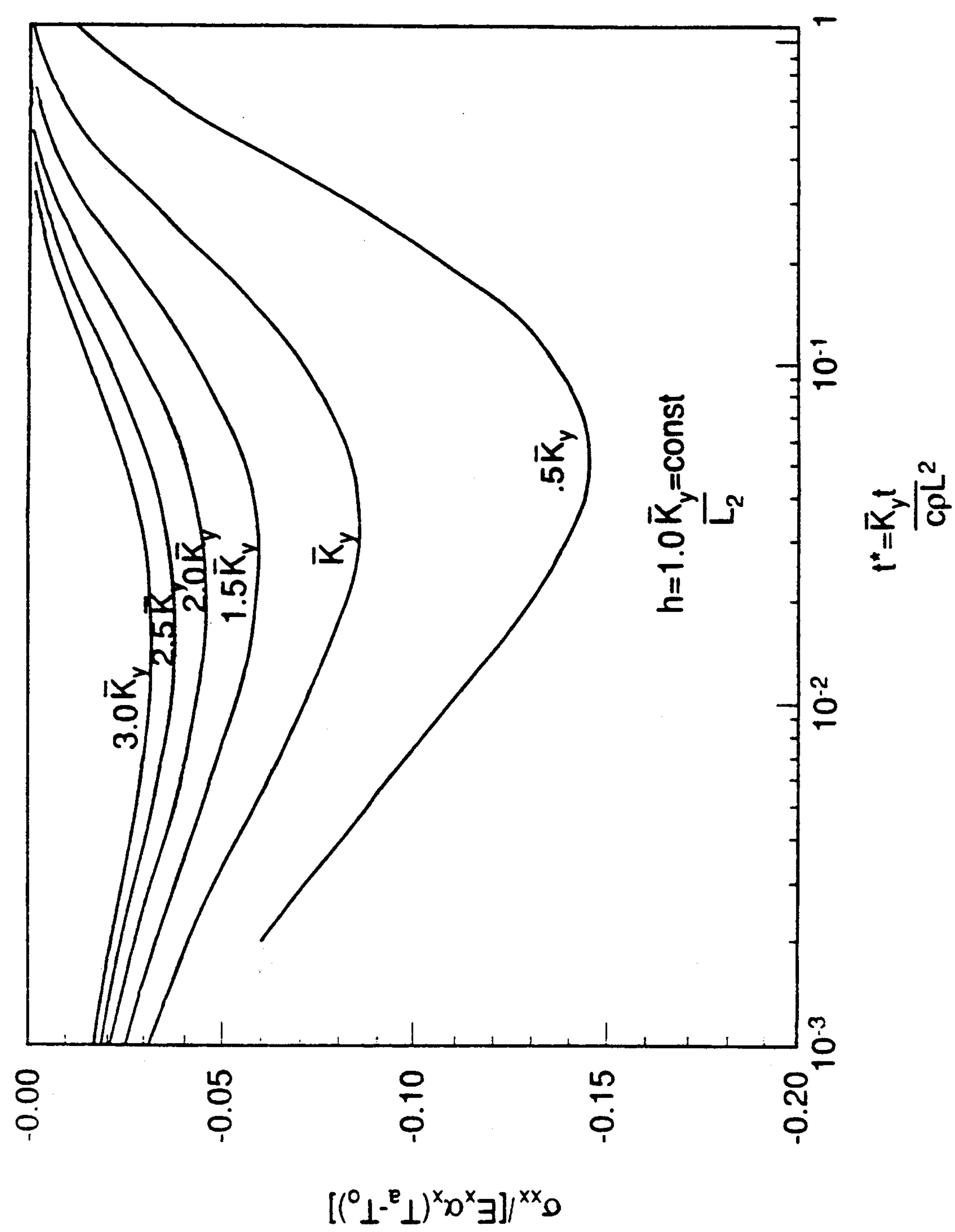

Figure 15

Typical Stress-Strain Response
for Sumitomo Reinforced Aluminosilicate

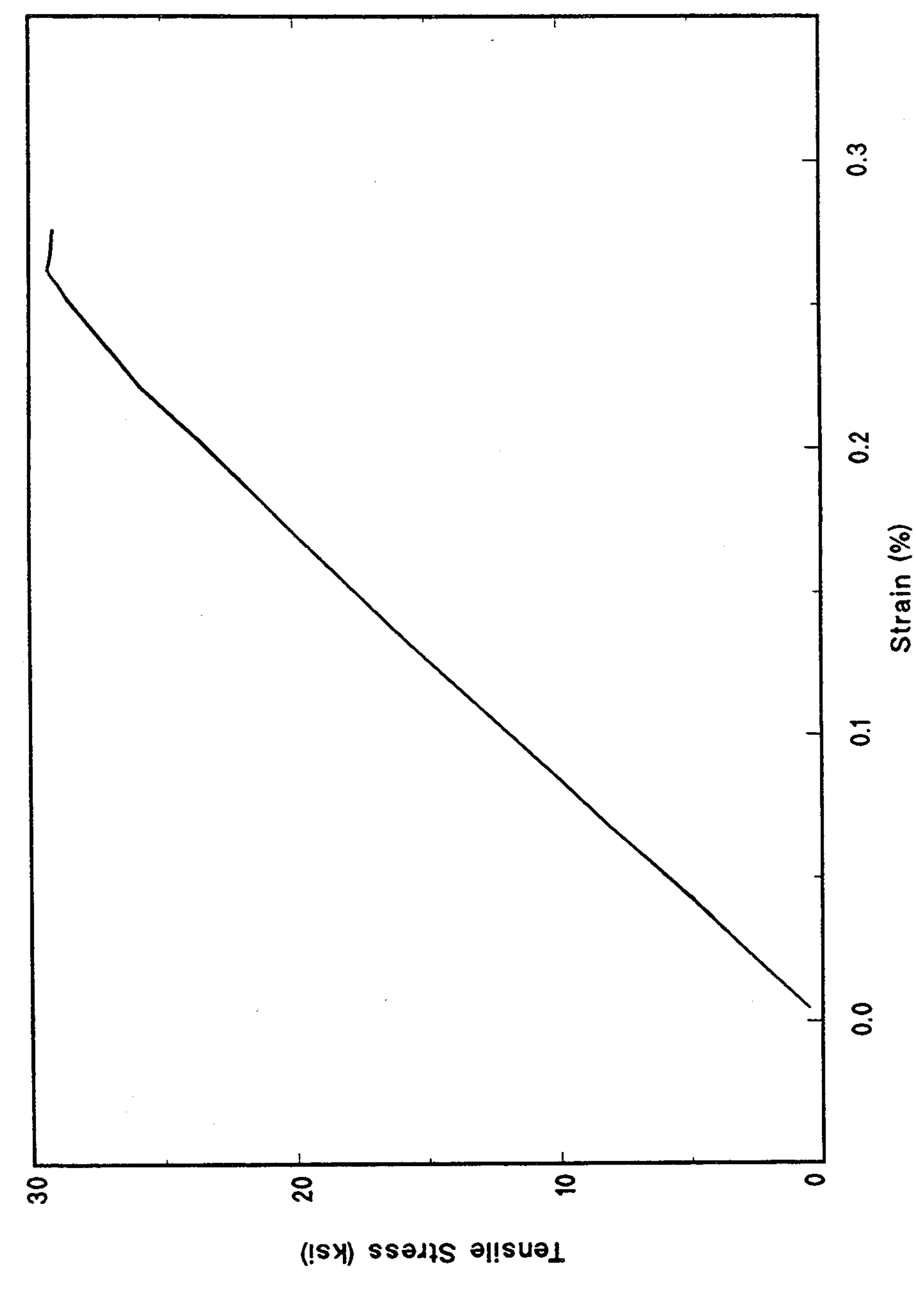

Figure 16

Surface Damage Indications for Sumitomo/Aluminosilicate Thermal Shock Sample (Shock-down/Severe/100 cycles)

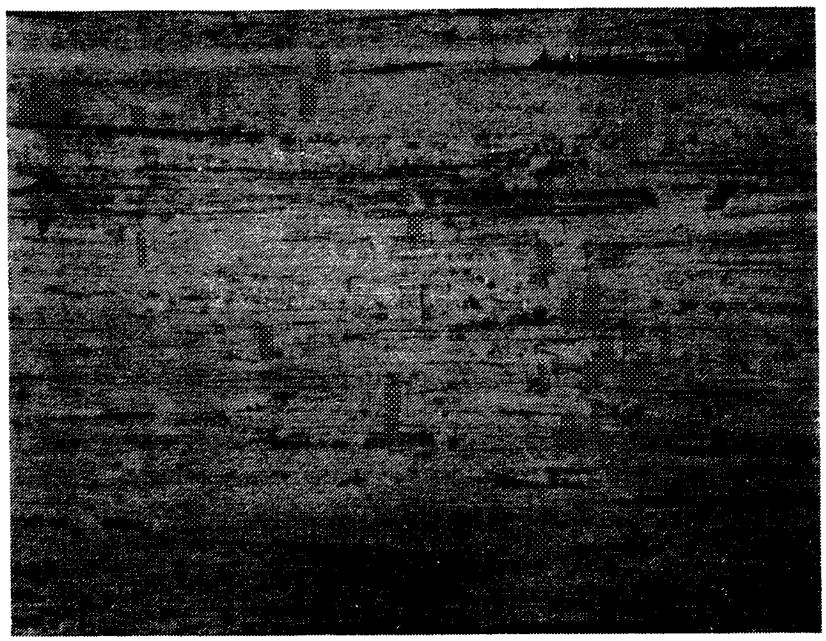

6X

Figure 17

Surface Damage Indications for Sapphire/Aluminosilicate Thermal Shock Sample (Shock-down/Severe/100 cycles)

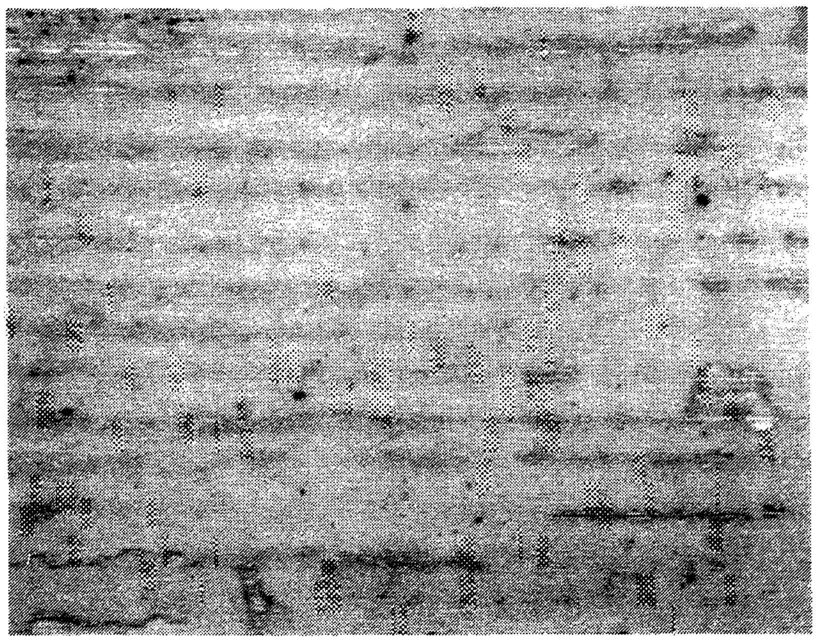

6X

Figure 18

Post-Shock Compressive Strength
Sumitomo/Aluminosilicate

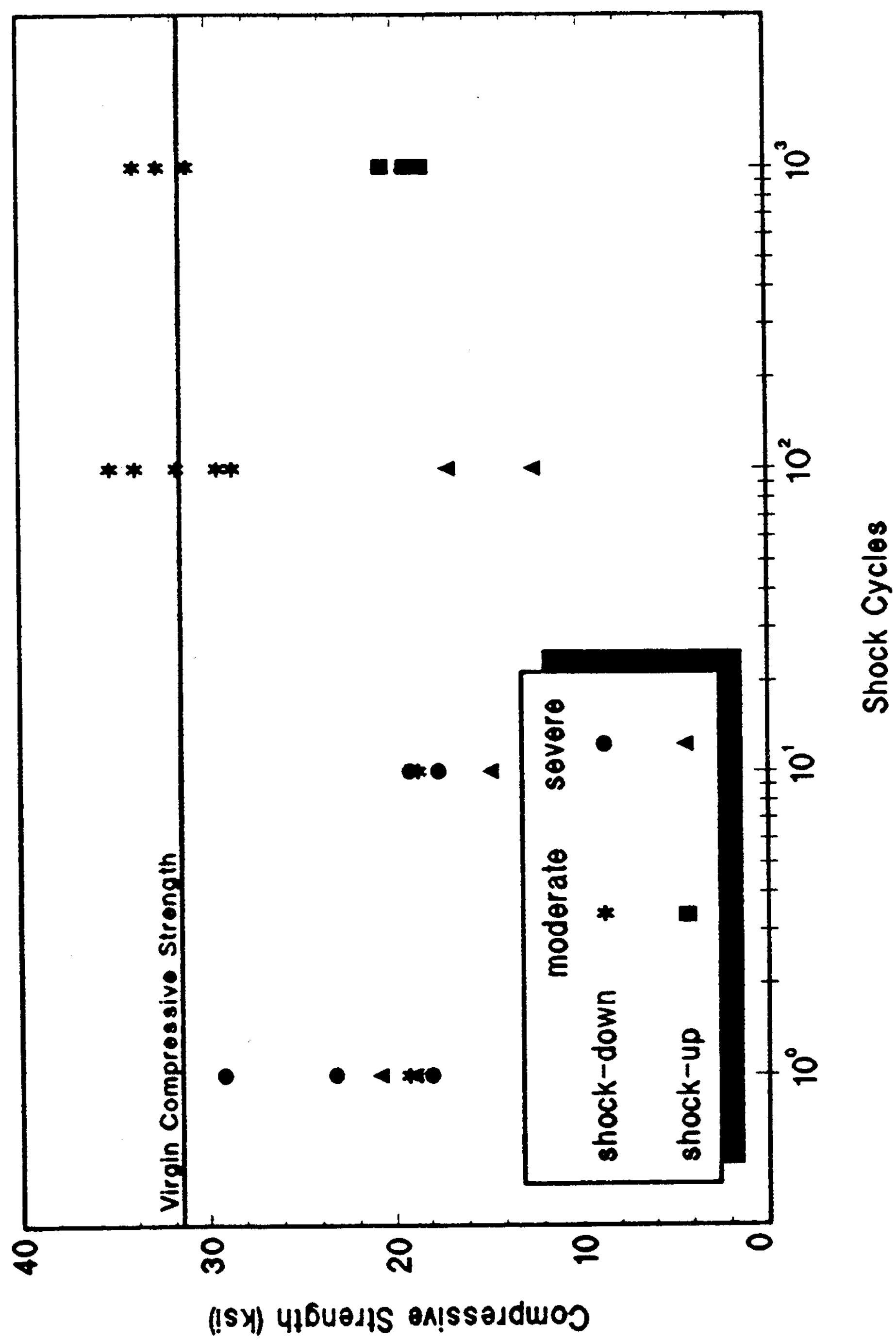

Figure 19

Post-Shock Compressive Strength
Sapphire/Aluminosilicate

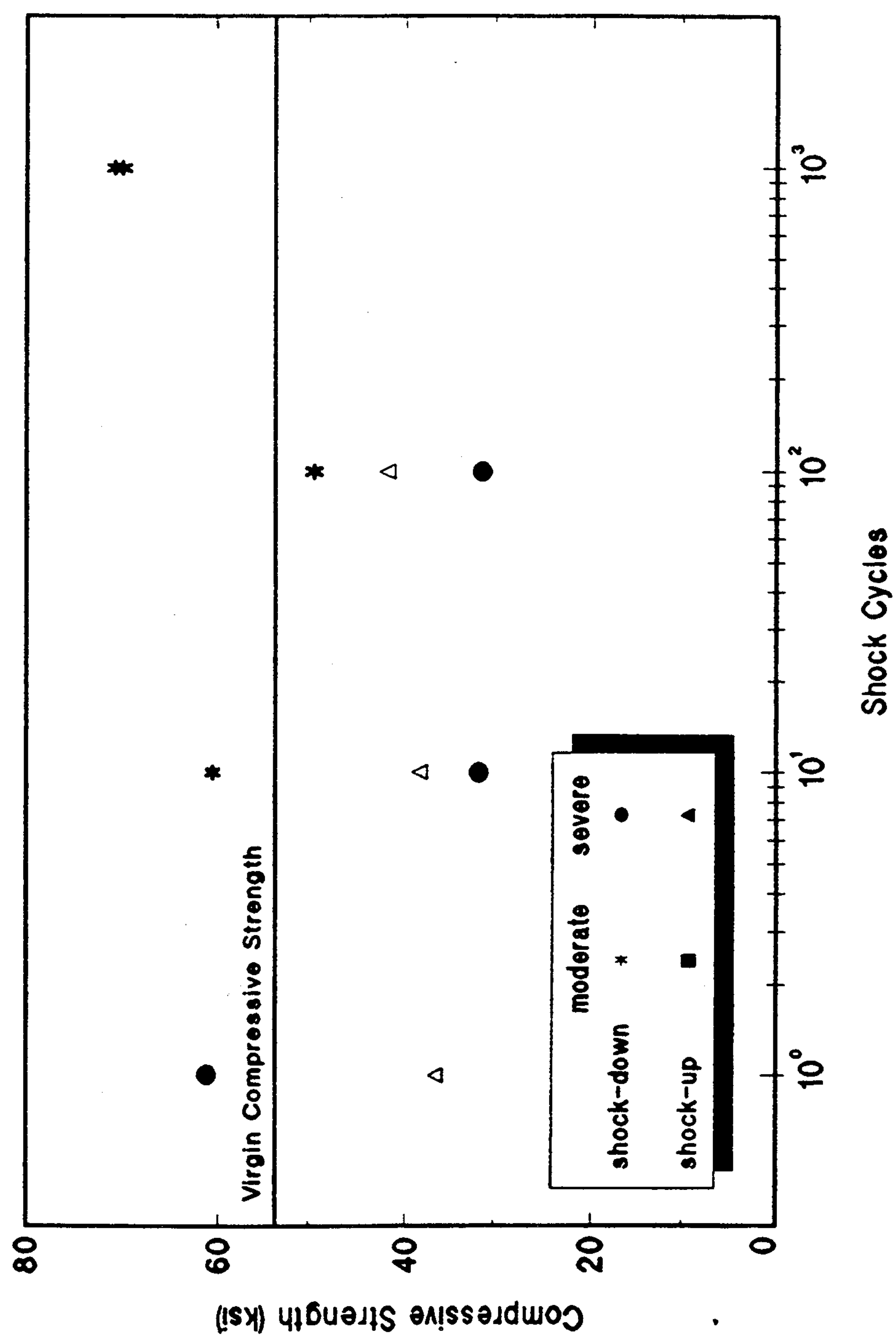

Figure 20

Post-Shock Microstructure
Sumitomo/Aluminosilicate

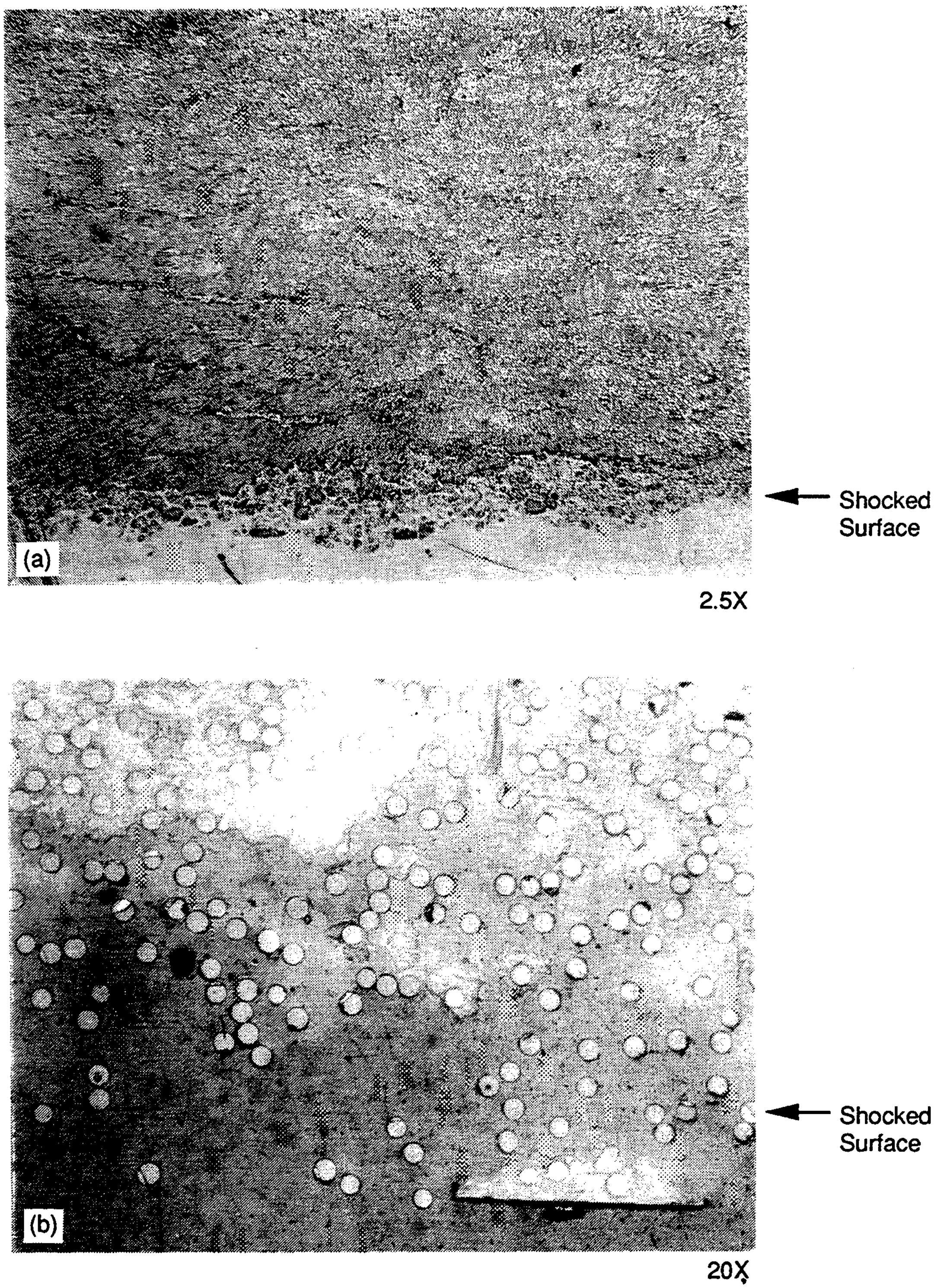

Figure 21

Post-Shock Microstructure
Sapphire/Aluminosilicate

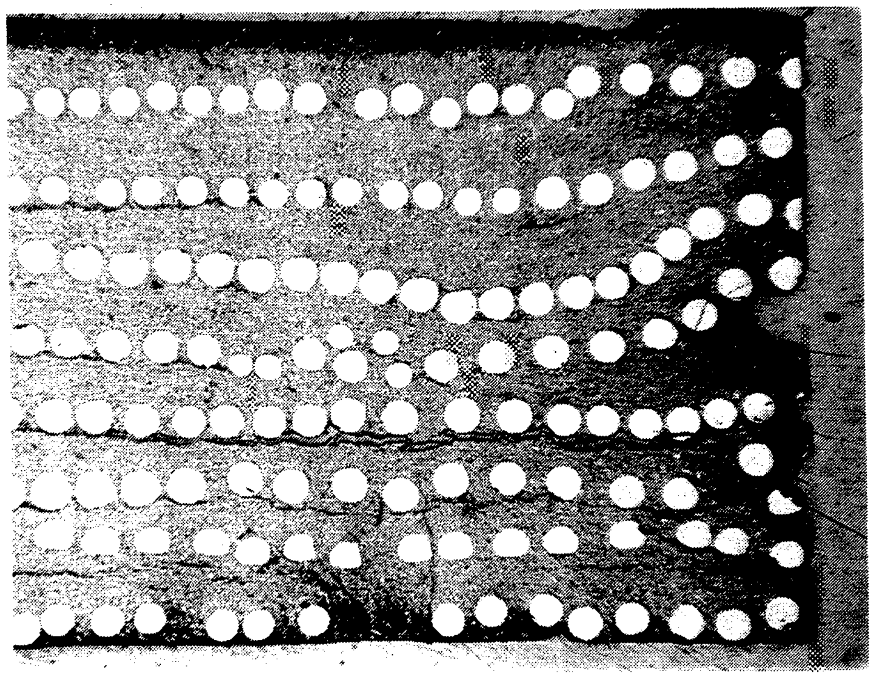

REPORT DOCUMENTATION PAGE

Form Approved
OMB No. 0704-0188

1. AGENCY USE ONLY (*Leave blank*)

2. REPORT DATE
August 1993

3. REPORT TYPE AND DATES COVERED
Final Contractor Report

4. TITLE AND SUBTITLE
Thermal Shock Resistance of Ceramic Matrix Composites

5. FUNDING NUMBERS
WU–510–01–50
NAS3–25640

6. AUTHOR(S)
D.M. Carper and H.F. Nied

7. PERFORMING ORGANIZATION NAME(S) AND ADDRESS(ES)
GE Aircraft Engines
Cincinnati, OH 45215–6301

8. PERFORMING ORGANIZATION REPORT NUMBER
E–8070

9. SPONSORING/MONITORING AGENCY NAME(S) AND ADDRESS(ES)
National Aeronautics and Space Administration
Lewis Research Center
Cleveland, Ohio 44135–3191

10. SPONSORING/MONITORING AGENCY REPORT NUMBER
NASA CR–189136

11. SUPPLEMENTARY NOTES
Project Manager, Mark J. Hyatt, Materials Division, (216) 433–3248.

12a. DISTRIBUTION/AVAILABILITY STATEMENT
Unclassified - Unlimited
Subject Category 24

12b. DISTRIBUTION CODE

13. ABSTRACT ***(Maximum 200 words)***

This report details the experimental and analytical investigation of the thermal shock phenomena in ceramic matrix composites. The composite systems examined were oxide-based, consisting of an aluminosilicate matrix with either polycrystalline aluminosilicate or single crystal alumina fiber reinforcement. The program was divided into three technical tasks; baseline mechanical properties, thermal shock modeling, and thermal shock testing. The analytical investigation focused on the development of simple expressions for transient thermal stresses induced during thermal shock. The effect of various material parameters, including thermal conductivity, elastic modulus, and thermal expansion, were examined analytically for their effect on thermal shock performance. Using a simple maximum stress criteria for each constituent, it was observed that fiber fracture would occur only at the most extreme thermal shock conditions and that matrix fracture, splitting parallel tot he reinforcing fiber, was to be expected for most practical cases. Thermal shock resistance for the two material systems was determined experimentally by subjecting plates to sudden changes in temperature on one surface while maintaining the opposite surface at a constant temperature. This temperature change was varied in severity (magnitude) and in number of shocks applied to a given sample. The results showed that for the most severe conditions examined that only surface matrix fracture was present with no observable fiber fracture. The impact of this damage on material performance was limited to the matrix dominated properties only. Specifically, compression strength was observed to decrease by as much as 50% from the measured baseline.

14. SUBJECT TERMS
Ceramics; Composites; Thermal shock; Thermal stress

15. NUMBER OF PAGES
43

16. PRICE CODE
A03

17. SECURITY CLASSIFICATION OF REPORT	18. SECURITY CLASSIFICATION OF THIS PAGE	19. SECURITY CLASSIFICATION OF ABSTRACT	20. LIMITATION OF ABSTRACT
Unclassified	Unclassified	Unclassified	